

Parameterization and benchmarking of the Modified Marrone-Treanor Model for five-species air*

Erik Torres[†], Thomas Gross[‡], Graham V. Candler[§] and Thomas E. Schwartzentruber[¶]
Department of Aerospace Engineering and Mechanics, University of Minnesota
107 Akerman Hall, 110 Union St SE, Minneapolis, MN, 55455

We present updated parameters for five-species air to be used with the Modified Marrone-Treanor (MMT) air dissociation model. The vibrational relaxation and chemical reaction rates are derived from quasiclassical trajectory calculation (QCT) and direct molecular simulation (DMS) using ab initio potential energy surfaces (PESs). The resulting model and parameter set enable efficient computational fluid dynamics (CFD) simulations of high-temperature nonequilibrium five-species air (N₂, O₂, NO, N and O). Through a consistent comparison, we show that the MMT model reproduces DMS benchmark solutions with high accuracy in zero-dimensional heat bath simulations representative of thermochemical nonequilibrium post-shock conditions. The MMT model's analytical expressions for dissociation rate coefficient and vibrational energy change per reaction ensure that the correct amount of energy is transferred between the vibrational and trans-rotational modes. Detailed balance is imposed for three-body recombination reactions and MMT solutions exhibit both quasi-steady-state (QSS) dissociation rates and proper approach to thermochemical equilibrium. MMT model predictions are compared to the Park two-temperature model for similar heat bath conditions. MMT predicts significantly slower conversion of N₂ into N below 10 000 K and significantly more NO production at all temperatures.

Nomenclature

a_U	=	fitting constant in MMT model [-]
\mathcal{A}_s	=	species s chemical symbol in reaction equation [-]
C	=	modified Arrhenius pre-exponential factor coefficient [$\text{cm}^3 \text{s}^{-1} \text{mol}^{-1} \text{K}^{-n}$]
c_v^t	=	specific constant-volume heat capacity of translational mode [$\text{J kg}^{-1} \text{K}^{-1}$]
c_v^r	=	specific constant-volume heat capacity of rotational mode [$\text{J kg}^{-1} \text{K}^{-1}$]

*Portions of this work were presented as paper 2023-3489 at the AIAA Aviation forum held in San Diego, CA

[†]Research Associate; etorres@umn.edu

[‡]Research Associate, AIAA member

[§]McKnight Presidential Endowed Chair, AIAA Fellow

[¶]Professor, AIAA Associate Fellow

$e_{v,s}$	=	species s specific vibrational energy [J kg^{-1}]
D	=	set of diatomic species $\{\text{N}_2, \text{O}_2, \text{NO}\}$
S	=	set of air species $\{\text{N}_2, \text{O}_2, \text{NO}, \text{N}, \text{O}\}$
E_v	=	mixture vibrational energy per unit volume [J m^{-3}]
E_v	=	mixture vibrational energy per unit volume [J m^{-3}]
f_k^{NB}	=	rate coefficient non-Boltzmann factor [-]
$f_\varepsilon^{\text{NB}}$	=	vibrational energy change non-Boltzmann factor [-]
h	=	specific enthalpy [J kg^{-1}]
\underline{I}	=	identity matrix [-]
k_{arr}	=	modified Arrhenius reaction rate coefficient [$\text{cm}^3 \text{s}^{-1} \text{mol}^{-1}$]
k_B	=	Boltzmann constant = $1.38065 \times 10^{-23} \text{J}$
k_d	=	effective dissociation rate coefficient [$\text{cm}^3 \text{s}^{-1} \text{mol}^{-1}$]
k_r^f, k_r^b	=	forward and backward rate coefficient for reaction r [$\text{cm}^3 \text{s}^{-1} \text{mol}^{-1}$]
K_r^{eq}	=	reaction r equilibrium constant [$(\text{mol}/\text{cm}^3)^{\nu_{\text{T},r}}$]
M_s	=	species s molar mass [kg kmol^{-1}]
$m_{s,q}^{\text{high}}, m_{s,q}^{\text{low}}$	=	high- and low-temperature limit slope parameters for $\log(\tau \cdot p)$ fit [$\text{K}^{1/3}$]
$n_{s,q}^{\text{high}}, n_{s,q}^{\text{low}}$	=	high- and low-temperature limit offset for $\log(\tau \cdot p)$ fit [-]
n	=	modified Arrhenius pre-exponential factor temperature exponent [-]
p	=	pressure [Pa], [atm]
Q_v^{relax}	=	translation-vibration energy relaxation source term [W m^{-3}]
Q_v^{chem}	=	vibrational energy-chemistry coupling source term [W m^{-3}]
\vec{q}_{tr}	=	trans-rotational energy heat flux [W m^{-2}]
\vec{q}_v	=	vibrational energy heat flux [W m^{-2}]
Q	=	approximate vibrational partition function [-]
R	=	set of chemical reactions [-]
S	=	mixture set of chemical species [-]
t	=	time [s]
T_t	=	mixture translational temperature [K]
T_r	=	mixture rotational temperature [K]
$T_{r,s}$	=	species s rotational temperature [K]
T_{t-r}, T	=	mixture trans-rotational temperature [K]
T_v	=	mixture vibrational temperature [K]

$T_{v,s}$	=	species s vibrational temperature [K]
$T_{D,s}$	=	species s dissociation temperature [K]
\vec{u}	=	flow velocity [m s^{-1}]
\vec{v}_s	=	species diffusion velocity [m s^{-1}]
w_s	=	species s mass production source term [$\text{kg s}^{-1} \text{m}^{-3}$]
x_s	=	species s mole fraction [-]
Z	=	vibrational nonequilibrium rate factor [-]
ρ_s	=	species s density [kg m^{-3}]
$\langle \tau_s^v \rangle$	=	species s average vibrational relaxation time [s]
$\tau_{s,q}^v$	=	relaxing species s vibrational relaxation time with collision partner species q [s]
$\langle \Delta \varepsilon_{v,s} \rangle_r$	=	species s vibrational energy <i>change</i> per reaction r [J kmol^{-1}]
$\langle \varepsilon_{v,s} \rangle_d$	=	per-particle vibrational energy removed for species s due to dissociation [eV]
$\Theta_{v,s}$	=	species s characteristic temperature of vibration [K]
$\nu'_{s,r}, \nu''_{s,r}$	=	species s stoichiometric coefficient before and after reaction r [-]
ρ_s	=	species s density [kg m^{-3}]
$\langle \tau_s^v \rangle$	=	species s mixture-averaged vibrational relaxation time [s]
$\underline{\tau}$	=	viscous stress tensor [Pa]

I. Introduction

THIS article presents a full parameterization of the Modified Marrone-Treanor (MMT) model for coupled internal energy relaxation and dissociation in five-species air (N_2 , O_2 , NO , N and O). Models like this are needed for performing computational fluid dynamics (CFD) simulations of high temperature air flows where the gas exists in thermal and chemical nonequilibrium, such as those found in hypersonic flow. Many hypersonic thermochemical models in the literature are parameterized by fitting results to shock-tube (or other) experimental data, which often are affected by significant uncertainty.

In recent decades an alternative approach has emerged, which relies on computational chemistry methods to generate reaction rate data essentially devoid of empiricism. It begins with the construction of ab initio potential energy surfaces (PESs) that dictate the instantaneous forces between colliding molecules arbitrarily arranged in physical space. At present, upward of 20 distinct PESs have been developed to predict the dynamics between the most relevant collision partners in five-species air (N_2 , O_2 , NO , N and O) in their respective ground electronic states. These PESs were purpose-built for simulating inelastic and reactive collisions, because they explicitly allow for stretching, breaking and re-forming of chemical bonds between the colliding atoms. All PESs employed to arrive at the rate parameters

presented in this work were originally generated by the University of Minnesota Computational Chemistry group [1–10] and can be found online [11].

Time integration of the classical equations of motion on these surfaces from an initial to a final molecular arrangement of point masses (usually 4-atom or 3-atom systems) is referred to as quasiclassical trajectory (QCT) calculations [12]. After a sweep is conducted over a suitable range of initial internal and relative collision energies (for instance, sampled from prescribed single-temperature, or (T, T_v) Boltzmann distributions) and the post-collision states are analyzed, reaction rate coefficients and average internal energy change per reaction, can be estimated [2, 13]. Statistical noise inherent to the Monte-Carlo sampling of initial conditions is driven down by performing trajectory calculation batches of larger size. In Ref. [14] an extensive QCT dataset for oxygen and nitrogen dissociation with N_2 , O_2 , N and O as collision partners was analyzed, resulting in the formulation and initial parameterization of the Modified Marrone-Treanor (MMT) dissociation model.

A different use-case for such interaction potentials is to employ them within the framework of the direct simulation Monte-Carlo [15] (DSMC) algorithm during the particle collision phase. This effectively produces a gas-kinetic flow simulation method, wherein the standard DSMC models for molecule-molecule scattering, internal energy relaxation and chemistry have been entirely replaced by on-the-fly trajectory calculations on highly accurate potentials. The idea was originally proposed by Koura [16], but it took until the emergence of suitable ab initio PESs for it to become viable for accurately simulating the high-temperature chemistry in nitrogen [17–19], oxygen [20–22] and finally five-species air mixtures [23–25]. In its current form it is referred to as Direct Molecular Simulation [26] (DMS) and represents a method able to simulate high-temperature nonequilibrium reacting flows essentially from first principles, including non-Boltzmann chemistry effects. Reference [26] gives an overview of the method and presents several verification test cases.

Due to its high computational cost, DMS has been mostly employed to study space-homogeneous adiabatic and isothermal heat baths. However, such a geometrically simple setup is ideal for studying nonequilibrium chemistry of air isolated from any interference due to flow effects (e.g. species diffusion, viscous dissipation, etc.). In this work we use DMS solutions in two complementary ways. First, to propose and calibrate the non-Boltzmann correction factors in the MMT model (see Sec. V in Ref. [14] and Secs. II.C-II.D in this work) as well as derive characteristic vibrational relaxation time parameters for air mixture components (see Ref. [24] and Sec. II.B in this work). Second, to produce benchmark test cases against which CFD solutions with the MMT model will be compared. Since the DMS benchmarks and MMT parameters are both derived from the same set of ab initio PESs, close agreement between solutions obtained with the two methods constitutes the actual metric of success for this effort. This approach replaces traditional model validation, because nowhere in the process do we rely on experimental data.

This work follows a recent article [14] that described the MMT model formulation and parameterized the model for a subset of species pairs. It also follows two recent articles (Refs. [23] and [24]) that presented new recommended

vibrational relaxation time- and reaction rate calculations corresponding to all current PESs that are available for five species air, where all results were derived from quasiclassical trajectory (QCT) calculations and direct molecular simulations (DMS) on ab initio PESs. Therefore, this article is best read in conjunction with the cited references.

The two main objectives of this paper are to present all internal energy relaxation and MMT model parameters for 5-species air and to compare its CFD implementation against DMS reference solutions at conditions representative of shock-heated air in hypersonic flows. As described in Sec. II.A, only the species conservation and vibrational energy balance equations are directly affected by the nonequilibrium chemistry model. Therefore, simple isothermal and adiabatic heat bath calculations are sufficient for benchmarking the model's behavior.

This paper is organized as follows. Section II provides a listing of the most up-to-date internal energy relaxation and chemical reaction rate parameters for the Modified Marrone-Treanor model, consistent with the formulation presented in Ref. [14]. In Sec. III we compare our CFD implementation of MMT for 5-species air against DMS reference solutions in a variety of relevant scenarios. For a meaningful comparison, it is important that all model parameters for thermodynamics, vibrational relaxation and air chemistry are directly derived from, or fully consistent with the ab initio PESs which DMS also relies upon. We test the nonequilibrium dissociation model in a full 5-species air mechanism, which includes updated QCT rates for the Zeldovich exchange reactions responsible for forming nitric oxide. Next, in Sec. IV we examine the effect of employing constant versus variable non-Boltzmann correction factors with the MMT model as the mixture approaches thermochemical equilibrium. In Sec. V we compare MMT predictions to assess the influence of the theorized multi-surface electronic energy enhancement factor for oxygen dissociation. Finally, in Sec. VI we compare MMT predictions to those obtained with Park's standard TT_v model [27] and in Sec. VII we formulate conclusions for this work. Additional details relevant for ensuring consistency between the model's implementation in CFD with the DMS reference calculations are discussed in the supplemental information.

II. Modified Marrone-Treanor model for air

In this section we summarize the model formulations and present full model parameterizations for vibrational energy relaxation times, reaction rate coefficients for the MMT model, and vibrational energy-chemistry coupling terms for the MMT model, along with the ab-initio data used to fit the parameters.

A. Governing equations for two-temperature chemistry CFD modeling

When flow of partially dissociated, but non-ionized air in thermo-chemical nonequilibrium is described by a two-temperature model, the Navier-Stokes equations take on the form:

$$\frac{\partial \rho_s}{\partial t} + \nabla \cdot (\rho_s \vec{u} + \rho_s \vec{v}_s) = w_s, \quad s \in S, \quad (1)$$

$$\frac{\partial \rho \vec{u}}{\partial t} + \nabla \cdot (\rho \vec{u} \otimes \vec{u} + p \underline{I} - \underline{\tau}) = \vec{0} \quad (2)$$

$$\frac{\partial E}{\partial t} + \nabla \cdot \left((E + p) \vec{u} - \underline{\tau} \vec{u} + \vec{q}_{tr} + \vec{q}_v + \sum_{s \in S} \rho_s h_s \vec{v}_s \right) = 0 \quad (3)$$

$$\frac{\partial E_v}{\partial t} + \nabla \cdot \left(E_v \vec{u} + \vec{q}_v + \sum_{s \in S} \rho_s e_{v,s} \vec{v}_s \right) = Q_v^{\text{relax}} + Q_v^{\text{chem}}, \quad (4)$$

with balance of species mass, momentum, total energy and vibrational-electronic energy described by Eqs. (1), (2), (3) and (4) respectively and $S = \{\text{N}_2, \text{O}_2, \text{NO}, \text{N}, \text{O}\}$ representing the set of five chemical species of the mixture.

The nonequilibrium chemistry model influences two parts of this system of equations. First, the calculation of the species mass production rates, on the right-hand side of Eq. (1):

$$w_s = M_s \sum_{r \in R} (v''_{s,r} - v'_{s,r}) \left(k_r^f \prod_{q \in S} \left(\frac{\rho_q}{M_q} \right)^{v'_{q,r}} - k_r^b \prod_{q \in S} \left(\frac{\rho_q}{M_q} \right)^{v''_{q,r}} \right), \quad s \in S, \quad (5)$$

where M_s is the molar mass of species s , R represents the set of reversible reactions, $v'_{s,r}$ and $v''_{s,r}$ represent the stoichiometric coefficients of species s in reaction r left and right of the reaction equation written in its generic form:



and k_r^f and k_r^b are the forward and backward rate coefficients for reaction r when read in the left-to-right sense. Backward and forward rate coefficients are linked via detailed balance relations $k_r^b = k_r^f / K_r^{eq}$, where K_r^{eq} represents the equilibrium constant for reaction r . Stoichiometric coefficients of species not participating in a given reaction are zero. In Sec. II.C we recall the functional form for the reaction rate coefficients and list the most up-to-date parameters in the MMT model for air. The second aspect of the fluid equations directly affected by the nonequilibrium model are the two source terms on the right hand side of Eq. (4). The functional form of the term Q_v^{relax} is given by Eq. (9) and the parameters for calculating the associated vibrational relaxation rates are presented later in Sec. II.B. The other source term, Q_v^{chem} , governs the conversion rate between vibrational-electronic and chemical potential energy. Its functional form is given by Eq. (18).

None of the inviscid, or viscous fluxes in the Navier-Stokes equations are influenced by the choice of gas-phase chemistry model and it becomes most convenient to test the implementation of such models separate from any interfering

flow effects. Thus, if one assumes zero spatial gradients for all state variables, Eqs. (1)-(4) reduce to a set of ordinary differential equations. The expressions for momentum and total energy balances become trivial, i.e. $d(\rho\vec{u})/dt = \vec{0}$ and $dE/dt = 0$ respectively, implying that $\rho\vec{u}$ and E remain constant over time and need not be solved for explicitly as part of the remaining ODE system:

$$\frac{d\rho_s}{dt} = w_s, \quad s \in S, \quad (7)$$

$$\frac{dE_v}{dt} = Q_v^{\text{relax}} + Q_v^{\text{chem}}. \quad (8)$$

These become the equations governing the time evolution of a constant-volume (isochoric), constant-total-energy (adiabatic) heat bath. This system of equations can be integrated in time for given initial conditions, typically specified in terms of an initial composition $\rho_{s,(t=0)}$, $\forall s \in S$ and initial temperatures $T_{(t=0)} \neq T_{v,(t=0)}$, which end up fixing the initial value of the total energy density $E = \frac{1}{2}\rho|\vec{u}|^2 + \rho e(T_{(t=0)}, T_{v,(t=0)})$ and the vibrational-electronic energy density $E_v = \rho e_v(T_{v,(t=0)})$. On the other hand, when the constraint $dE/dt = 0$ is dropped in favor of imposing a fixed value for the translation-rotational temperature $T = T_{(t=0)}$ at all times, Eqs. (7)-(8) describe the time evolution of a gas mixture in what we call a constant-volume (isochoric), constant-temperature (isothermal) heat bath. Both scenarios represent rather simplified and somewhat abstract nonequilibrium “flows fields”. They are useful nonetheless, because they allow us to study the effect of the chemistry model in isolation. Testing the CFD implementation of the MMT model in this way is especially convenient, because the first-principles benchmark solutions obtained with DMS are also obtained in equivalent space-homogeneous (0D) isothermal or adiabatic heat baths.

All CFD solutions employing the MMT or Park models in Secs. III-VI, are obtained using a standard explicit fourth-order Runge-Kutta ODE time integration scheme.

B. Vibrational relaxation times

In two-temperature nonequilibrium models relaxation of translational and vibrational modes toward thermal equilibrium is typically described by a source term Q_v^{relax} in the vibrational energy equation, i.e. Eq. (4) :

$$Q_v^{\text{relax}} = \sum_{s \in D} \rho_s \frac{e_{v,s}(T_{t-r}) - e_{v,s}(T_v)}{\langle \tau_s^v \rangle}, \quad (9)$$

consisting of a mixture-weighted sum over all vibrationally relaxing diatomic species $D = \{N_2, O_2, NO\}$. Each species’ contribution is modeled as a Landau-Teller relaxation term, where the numerator represents departure of that species’ vibrational energy $e_{v,s}(T_v)$ at local vibrational temperature T_v from the corresponding hypothetical equilibrium value at the local gas trans-rotational temperature $e_{v,s}(T_{t-r})$. The denominators in Eq. (9) represent each of the three relaxing diatomic species’ average vibrational relaxation times, themselves defined as averages over reciprocals of pair-wise

relaxation times $\tau_{s,q}^v$ weighted by mole fraction x_q of collision partner $q \in S$, with $S = \{\text{N}_2, \text{O}_2, \text{NO}, \text{N}, \text{O}\}$:

$$\langle \tau_s^v \rangle = \left(\sum_{q \in S} \frac{x_q}{\tau_{s,q}^v} \right)^{-1}, \quad s \in D, \quad (10)$$

For air species one would traditionally rely on the Millikan & White correlation [28] in conjunction with Park’s high-temperature correction [29] to determine these pair-wise relaxation times. However, experimental evidence [30–34] as well as recent first-principles calculations [20, 21, 24] have revealed significant discrepancies for some species pairings, especially in the high-temperature limit. In this paper we present an alternative expression together with the necessary fit parameters to calculate characteristic vibrational relaxation times for N_2 , O_2 and NO , which are derived from recent DMS calculations [24] using only ab initio PESs.

The analytical expression chosen to curve-fit the DMS-derived pair-wise vibrational relaxation times (repeated from Eq. (19) in Ref. [14]) has the form:

$$\tau_{s,q}^v = \frac{1}{p} \left(\exp \left(m_{s,q}^{\text{low}} T^{-1/3} + n_{s,q}^{\text{low}} \right) + \exp \left(m_{s,q}^{\text{high}} T^{-1/3} + n_{s,q}^{\text{high}} \right) \right), \quad s \in D, q \in S, \quad (11)$$

where s and q are species indices, p is the pressure and T is the trans-rotational temperature. This expression assumes that there are two distinct “low-temperature” and “high-temperature” limiting behaviors for each $\tau_{s,q}^v$, which can be parameterized by separate straight-line segments on a $\log(\tau_{s,q}^v \cdot p)$ vs. $T^{-1/3}$ plot.

Numerical parameters required to evaluate Eq. (11) for each individual relaxation pair are listed in Table 1 and the results are summarized in Fig. 1. Blue symbols represent the original DMS data from Ref. [24], while dashed blue lines show our corresponding curve fits. For comparison, the continuous black line in each sub-plot of Fig. 1 shows the corresponding prediction with the Millikan & White (M&W) correlation [28]. For some species pairs (e.g. for $s - q = \text{N}_2 - \text{N}_2$ and $\text{O}_2 - \text{O}_2$), the DMS predictions tend to agree well with the M&W correlations at lower temperatures, whereas for others the DMS behavior and experiments differ significantly from Millikan & White (for $\text{O}_2 - \text{O}$ in particular, also see Fig. 7 in Ref. [21]). For all species pairs the high-temperature relaxation behavior predicted by the M&W correlation deviates significantly from that observed in our DMS calculations. Dotted black curves representing the effect of adding Park’s high-temperature correction to the Millikan & White prediction are shown in Figs. 1(a), (c) and (j) for the three single-species interactions $s - q = \text{N}_2 - \text{N}_2$, $\text{O}_2 - \text{O}_2$ and $\text{NO} - \text{NO}$. This correction, as defined in the section entitled “Vibrational Relaxation Parameters” of Ref. [29], is applied to each of the three diatomic species’ overall relaxation times, i.e.: $1/\langle \tau_s^v \rangle^{\text{overall}} = 1/\langle \tau_s^v \rangle^{\text{M\&W}} + 1/\langle \tau_s^v \rangle^{\text{Park-HT}}$, after the Millikan & White portion itself has been calculated by weighting the pair-wise contributions according to Eq. (10). Each species-specific overall relaxation time is thus dependent on the given mixture composition. Conversely, the Park high-temperature correction cannot be applied to individual pair-wise relaxation times, but only to the combined

one as a whole. It therefore only makes sense to plot the correction for a particular mixture composition, or as done in this case, for the single-species interactions that simultaneously represent the overall relaxation time in a pure gas, i.e. $\langle \tau_s^v \rangle(x_s = 1) = \tau_{s,s}^v$. For all three single-species interactions, the Park high-temperature correction and the corresponding DMS-derived curve fits both depart upward from the linear-slope T -dependence at very high temperatures. However, the effect of the Park correction is far more pronounced than in any of the DMS-derived curve fits.

For species pairings $s - q = \text{N}_2 - \text{O}$, $\text{NO} - \text{N}$, $\text{NO} - \text{O}$ and $\text{NO} - \text{NO}$ a second set of red symbols and corresponding orange dashed lines are shown in Fig. 1. As discussed in Ref. [24], only a fraction of the PESs necessary for computing the relaxation times of these particular species pairings is currently available. At present we estimate them based on the subset of available potentials. The two curves shown represent our estimates based on the available data. The larger time constant estimates (blue symbols, blue dashed line) were obtained under the assumption that only trajectories on the available PESs contribute to vibrational relaxation for the species pair in question. The lower estimates (red symbols, orange dashed line) are obtained under the assumption that trajectories on the unavailable PESs contribute in the same manner to vibrational relaxation as the available ones. Note that for each species pairing the two sets of curves exhibit the exact same temperature dependence, only offset by a constant value along the ordinate axis. Both estimates are relevant to the work discussed in this paper. The dashed blue lines represent the relaxation behavior that is consistent with the reference DMS calculations used for model benchmarking purposes in Sec. III. Since these DMS calculations are subject to the same PES availability gaps, we employ the upper-end estimates when comparing CFD results against pure DMS (see footnote [b] in Table 1). By contrast, the orange dashed lines represent our best estimate for the vibrational relaxation times in a realistic air mixture. These alternative values are used in Sec. VI, where we make adjustments to the nonequilibrium model to improve its behavior for realistic hypersonic flows (see footnote [c] in Table 1) and compare its predictions against simulations employing M&W relaxation times together with the Park TT_v model [29].

Further note that in Fig. 1 plots for pairings $s - q = \text{N}_2 - \text{NO}$, $\text{O}_2 - \text{NO}$, $\text{NO} - \text{N}_2$ and $\text{NO} - \text{O}_2$ are missing entirely. No DMS data for these pairings could be generated in Ref. [24], as none of the prerequisite NO_3 and N_3O ab initio PESs currently exist. Thus, in the model comparisons against DMS in Sec. III we will assume that the respective relaxation times tend toward infinity (see footnote [a] in Table 1), mimicking the behavior of the DMS reference solutions. Note again that this approach makes sense only during the model benchmarking phase, but not so when the intention is to use CFD to simulate realistic hypersonic flows. For that scenario we re-purpose data from other available pairings as surrogates. The underlying assumption is that vibrational relaxation times of a particular species s will depend to a lesser degree on the collision partner species q . Thus, for pairing $s - q = \text{N}_2 - \text{NO}$ we choose to replace NO with N_2 as the collision partner and use the same curve fit values as for $\text{N}_2 - \text{N}_2$. In analogous fashion, for pairing $\text{O}_2 - \text{NO}$ we swap out NO for O_2 as collision partner and end up using the same parameters as for $\text{O}_2 - \text{O}_2$. Finally, for the

Table 1 DMS-derived fit parameters for pressure-weighted characteristic vibrational relaxation times [atm · s] evaluated according to Eq. (11)

Species pair $s - q$	m_l [K ^{1/3}]	n_l [-]	m_h [K ^{1/3}]	n_h [-]	note
N ₂ – N ₂	221.0	-24.83	33.30	-17.31	
N ₂ – O ₂	115.0	-20.25	-51.42	-15.26	
N ₂ – NO	— Re-use parameters for N ₂ – N ₂ —				[a]
N ₂ – N	239.4	-28.52	32.34	-18.39	
N ₂ – O*	149.5	-23.10	-1.201	-17.00	[b]
N ₂ – O**	149.5	-23.51	-1.201	-17.40	[c]
O ₂ – N ₂	134.0	-22.37	-0.7123	-16.95	
O ₂ – O ₂	129.0	-22.29	-4.384	-16.70	
O ₂ – NO	— Re-use parameters for O ₂ – O ₂ —				[a]
O ₂ – N	81.22	-21.16	9.111	-17.61	
O ₂ – O	3.018	-17.74	-121.6	-15.82	
NO – N ₂	— Re-use parameters for NO – NO** —				[a]
NO – O ₂	— Re-use parameters for NO – NO** —				[a]
NO – NO*	127.2	-20.72	-27.61	-14.06	[b]
NO – NO**	127.2	-23.20	-27.61	-16.55	[c]
NO – N*	64.31	-19.08	-62.33	-15.82	[b]
NO – N**	64.31	-20.06	-62.33	-16.80	[c]
NO – O*	-24.76	-15.37	-113.0	-18.91	[b]
NO – O**	-24.76	-17.16	-113.0	-20.70	[c]

[a] Relaxation time $\tau_{s,q}^v \rightarrow \infty$ when comparing against DMS benchmarks by setting $m_l = m_h = 0$ and $n_l = n_h$ to “very large” constant.

[b] Used only when comparing against DMS (MMT-benchmark)

[c] Used with full model for realistic conditions (MMT)

two remaining nitric oxide relaxation times NO – N₂ and NO – O₂, we apply the same principle and assume both relaxation times behave the same as the lower-bound estimate for NO – NO.

C. Reaction rate coefficients for MMT model

As shown in Ref. [14], in the Modified Marrone-Treanor model two-temperature dissociation rate coefficients are evaluated according to:

$$k_d^{\text{MMT-NB}}(T, T_v) = k_d^{\text{arr}} Z(T, T_v) f_k^{\text{NB}}, \quad (12)$$

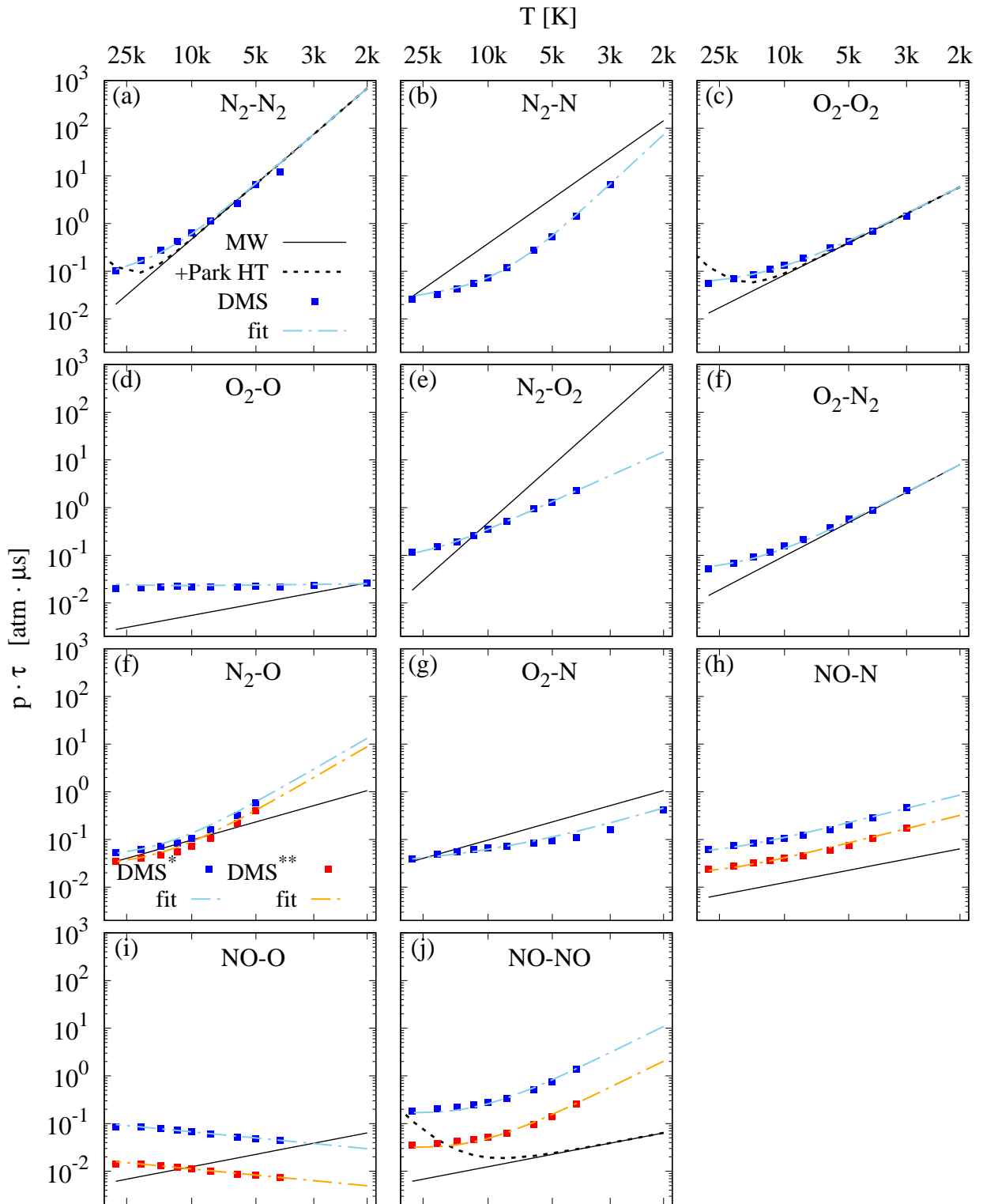


Fig. 1 Characteristic vibrational relaxation times for air species derived from DMS (blue symbols), corresponding fits according to Eq. (11) (dashed light blue lines), alternative estimates (red symbols and orange dashed lines), Millikan & White correlation (black solid lines) plus Park high-temperature correction (black dotted lines)

where k_d^{arr} represents the *thermal equilibrium* dissociation rate coefficient in modified Arrhenius form:

$$k_d^{\text{arr}}(T) = CT^n \exp(-E_a/k_B T), \quad (13)$$

while $Z(T, T_v)$ is the MMT model's vibrational nonequilibrium factor, as derived by Marrone and Treanor [35]:

$$Z(T, T_v) = \frac{Q(T) Q(T_F)}{Q(T_v) Q(-U)}, \quad (14)$$

and f_k^{NB} is a non-Boltzmann correction factor discussed in more detail in Secs. V and VI of Ref.[14]. The Q 's appearing in Eq. (12) are approximate vibrational partition functions of the form:

$$Q(T) = \frac{1 - \exp(-T_{D,s}/T)}{1 - \exp(-\Theta_{v,s}/T)} \quad (15)$$

and T_F and U are pseudo-temperatures defined as:

$$T_F(T, T_v) = \left(\frac{1}{T_v} - \frac{1}{T} - \frac{1}{U(T)} \right)^{-1} \quad (16)$$

and:

$$U(T) = \left(\frac{a_U}{T} + \frac{1}{U^*} \right)^{-1} \quad (17)$$

In this section we present the most up-to-date kinetic rate parameters to be used with the Modified Marrone-Treanor model. Note that what is referred to as “the MMT model” actually consists of multiple parts. First, the collection of Arrhenius rate parameters for 5-species air reactions fit to our most recent QCT calculations based on ab initio PESs. Second, all relevant expressions and fit parameters (see a_U, U^* in Eq. (17)) necessary to compute the vibrational nonequilibrium factor $Z(T, T_v)$ according to Eq. (14), average vibrational energy removed per dissociation $\langle \varepsilon_{v,s} \rangle_{\text{diss}}$ (see Eq. (20) in Sec. II.D) as well as the non-Boltzmann correction factors f_k^{NB} and $f_\varepsilon^{\text{NB}}$ during QSS dissociation. Only when all these components are integrated within the MMT model can it accurately predict nonequilibrium dissociation in a post-shock environment. It should further be mentioned that the MMT model, as presented in Ref. [14], was calibrated taking into account only a subset of all air reactions. This original dataset relied on QCT calculations by Bender et al. [2] and Chaudhry et al. [13, 36] for collision-induced N_2 -dissociation by impact with N_2 , N and O_2 , as well as O_2 -dissociation by impact with N_2 , O and O_2 . The Arrhenius and MMT parameters derived from the original calibration by Chaudhry et al. are listed for reference in Table 1 of Ref. [14].

New, more complete QCT and DMS calculations [23] incorporating the most up-to-date ab initio potentials complement these earlier results and, in some instances, now supersede them. Table 2 in this paper lists the updated

reaction set, split into dissociation-type reactions for the three diatomic species (rows 1 - 15), exchange-type, among them the two Zeldovich reactions $\text{N}_2 + \text{O} \rightleftharpoons \text{NO} + \text{N}$ and $\text{NO} + \text{O} \rightleftharpoons \text{O}_2 + \text{N}$ (rows 16 - 18) plus three remaining reactions of “mixed” dissociation/exchange type. The second-to-last column lists whether the rate coefficient and vibrational energy-chemistry coupling terms are computed according to the nonequilibrium MMT formulations given in Sec. II.B of Ref. [14], or whether a thermal rate constant and non-preferential vibrational energy-coupling is assumed for the given reaction. The last column lists the provenance of the associated QCT data. Our corresponding recommended kinetic rate parameters are listed in Table 3.

A careful comparison of Table 1 in Ref. [14] with Table 3 in this paper reveals different numerical values for the fit parameters of all common reactions listed. For the “pure” nitrogen and oxygen dissociation reactions (i.e. reactions 1, 4, 7 and 10 in Table 3) this is merely a consequence of having re-fitted the original QCT data of Bender et al. [2] and Chaudhry [36] to a two-parameter modified Arrhenius expression with dissociation temperatures ($T_D = E_a/k_B$) held fixed to the standard values $T_{D,\text{N}_2} = 113\,200\text{ K}$ and $T_{D,\text{O}_2} = 59\,330\text{ K}$ respectively. The associated MMT parameters a_U and U^* also differ slightly between both tables, because updated values for the characteristic vibrational temperatures ($\Theta_{v,\text{N}_2} = 3414\text{ K}$ and $\Theta_{v,\text{O}_2} = 2251\text{ K}$) were used in the latter. In addition to these minor changes it became necessary to update the Arrhenius and MMT parameters for both “mixed” $\text{N}_2 - \text{O}_2$ dissociation reactions (i.e. compare reactions 2 and 6 in Table 3 vs. rows 3 and 6 of Table 1 in Ref. [14]), because the N_2O_2 potential was recently re-fitted (most recent PES source employed is `N2O2_3A_MB-PIP-MEG2` vs. older source `PES_N2O2_triplet_umn_v1` on potlib [11]). This resulted in small, but still noticeable changes to the QCT rate coefficients relative the ones obtained by Chaudhry et al. [13] with the older version of the PES.

1. MMT parameters for comparison against DMS results

As discussed in Ref. [23], a fraction of the ab initio PESs necessary to generate the full set of ground-electronic-state 5-species air reactions from QCT calculations currently does not exist. This problem partially affects reactions 5, 14, 15 and 19-20 in Table 3, but especially the entirely missing PESs for reactions involving $\text{N}_2 - \text{NO}$ and $\text{O}_2 - \text{NO}$ collision pairs (reactions 3, 8, 11 and 12). We deal with these limitations differently depending on whether we are comparing the model against DMS results, or proposing the model for realistic air simulations. In Sec. III, where we perform several calculations to test the MMT model’s ability to reproduce a series of DMS reference results, we adjust the CFD reaction set from Table 2 to exclude reactions 3, 8, 11 and 12, as these do not take place in the DMS calculations. Furthermore, the DMS reference calculations currently are not set up to simulate any reactions involving three simultaneous collision partners as reactants. Thus, none of the reverse reactions of the dissociation-type (reactions 1-15) nor of the “mixed” exchange-dissociation (reactions 19-21) are taken into account in the DMS reference results. As a consequence, in Sec. III we explicitly model all aforementioned reactions as irreversible in the forward direction. The only exceptions are the three exchange reactions (reactions 16-18 in Table 2). Since both their forward and backward partial reactions

involve only two colliding particles as reactants, they both are included in our DMS solutions and consequently also in the corresponding CFD calculations. For these three reactions the reverse rate coefficients are calculated using standard detailed balance relations and the relevant equilibrium constants. We should also note that during the process of comparing our MMT results against DMS we evaluate the rate coefficients of all oxygen dissociation reactions (6-10 in Table 2) explicitly *without* the multi-electronic-surface enhancement factor $\eta = 16/3$ (See Refs. [21] and [37] (pp. 331-334) for the reasoning behind proposing this factor). During the model benchmarking stage this is the correct choice, since our DMS calculations only account for reactions involving oxygen molecules in their ground electronic state.

2. MMT parameters proposed for full 5-species air simulations

The MMT parameters for realistic dissociating air simulations must include all possible collision pairs in a 5-species air mixture. Here we fill in the aforementioned gaps for dissociation reactions involving nitric oxide by re-using rate data from other, similar reactions. Specifically, reaction 3 in Tables 2 and 3 uses the same parameters as reaction 1, while reaction 8 relies on the same parameters as reaction 7. Finally, both for reactions 11 and 12 we assume the same rate parameters as for reaction 13. We now also include the possibility for all reactions in Table 2 to be reversible by imposing detailed balance relations, as discussed in Sec. VI of Ref. [14]). Finally, we must now take into account the effect of electronically excited states of molecular oxygen on the dissociation rate. Essentially, we consider two limiting cases. One assumption, discussed in Refs. [21] and [37] (pp. 331-334), states that behind strong shocks all electronic excited states of O_2 lying between its ground state energy and its dissociation threshold of 5.213 eV become Boltzmann-populated and enhance the overall dissociation rates well beyond that of O_2 populating the ground state alone. The scaling proposed is to assume the ground state $O_2(X^3\Sigma_g^-)$ and all excited states in question contribute according to their respective degeneracies $3 + 2 + 1 + 1 + 6 + 3$ (first six rows in Table I of Ref. [21]) to augment the ground-state-only dissociation rate (hence $\eta = 16/3$). Thus, in this limit we modify all reaction rate coefficients involving O_2 as the dissociating species (reactions 6 - 10 in Table 2) to have their pre-exponential Arrhenius terms augmented by the multi-electronic surface factor $\eta = 16/3$ when simulating realistic flow conditions. The other limiting case is to assume none of the excited states are populated and the overall O_2 dissociation rate will be equal that of the ground state alone. Thus, no enhancement factor would be used. To the authors' best knowledge there are at present no ab initio results in the literature to fully support either assumption and we merely present both options as the two limiting cases. We therefore note that the MMT model can be used with, or without these enhancement factors. In our comparison calculations against the Park model in Sec. VI, we present MMT results with and without the factor applied.

In Fig. 2 we now collect Arrhenius plots of all reactions from Tables 2 and 3 for which ab initio QCT data is available (i.e. all except for 3, 8, 11 and 12). All QCT-derived *thermal equilibrium* rate coefficients are shown as black

Table 2 Reaction types included in updated MMT model (2024 version) for direct comparison with DMS.

	Type	Reaction	Model	QCT rates source
1	diss	$\text{N}_2 + \text{N}_2 \rightleftharpoons \text{N} + \text{N} + \text{N}_2$	MMT	Bender et al [2]
2	diss	$\text{N}_2 + \text{O}_2 \rightleftharpoons \text{N} + \text{N} + \text{O}_2$	MMT	Torres et al [23]
3	diss	$\text{N}_2 + \text{NO} \rightleftharpoons \text{N} + \text{N} + \text{NO}$	re-use (1) [a]	no dedicated QCT data
4	diss	$\text{N}_2 + \text{N} \rightleftharpoons \text{N} + \text{N} + \text{N}$	MMT	Bender et al[2]
5	diss	$\text{N}_2 + \text{O} \rightleftharpoons \text{N} + \text{N} + \text{O}$	MMT	Torres et al [23] (partial PESs)
6	diss	$\text{O}_2 + \text{N}_2 \rightleftharpoons \text{O} + \text{O} + \text{N}_2$	MMT [b]	Torres et al [23]
7	diss	$\text{O}_2 + \text{O}_2 \rightleftharpoons \text{O} + \text{O} + \text{O}_2$	MMT [b]	Chaudhry et al [13]
8	diss	$\text{O}_2 + \text{NO} \rightleftharpoons \text{O} + \text{O} + \text{NO}$	re-use (7) [a,b]	no dedicated QCT data
9	diss	$\text{O}_2 + \text{N} \rightleftharpoons \text{O} + \text{O} + \text{N}$	MMT [b]	Torres et al [23]
10	diss	$\text{O}_2 + \text{O} \rightleftharpoons \text{O} + \text{O} + \text{O}$	MMT [b]	Chaudhry et al [13]
11	diss	$\text{NO} + \text{N}_2 \rightleftharpoons \text{N} + \text{O} + \text{N}_2$	re-use (13) [a]	no dedicated QCT data
12	diss	$\text{NO} + \text{O}_2 \rightleftharpoons \text{N} + \text{O} + \text{O}_2$	re-use (13) [a]	no dedicated QCT data
13	diss	$\text{NO} + \text{NO} \rightleftharpoons \text{N} + \text{O} + \text{NO}$	thermal/non-pref.	Torres et al [23]
14	diss	$\text{NO} + \text{N} \rightleftharpoons \text{N} + \text{O} + \text{N}$	MMT	Torres et al [23] (partial PESs)
15	diss	$\text{NO} + \text{O} \rightleftharpoons \text{N} + \text{O} + \text{O}$	MMT	Torres et al [23] (partial PESs)
16	exch	$\text{N}_2 + \text{O} \rightleftharpoons \text{NO} + \text{N}$	thermal/non-pref.	Torres et al [23]
17	exch	$\text{NO} + \text{O} \rightleftharpoons \text{O}_2 + \text{N}$	thermal/non-pref.	Torres et al [23]
18	exch	$\text{N}_2 + \text{O}_2 \rightleftharpoons 2\text{NO}$	thermal/non-pref.	Torres et al [23]
19	mixed	$\text{NO} + \text{NO} \rightleftharpoons \text{O} + \text{O} + \text{N}_2$	thermal/non-pref.	Torres et al [23] (partial PESs)
20	mixed	$\text{NO} + \text{NO} \rightleftharpoons \text{N} + \text{N} + \text{O}_2$	thermal/non-pref.	Torres et al [23] (partial PESs)
21	mixed	$\text{N}_2 + \text{O}_2 \rightleftharpoons \text{NO} + \text{N} + \text{O}$	thermal/non-pref.	Torres et al [23]

[a] Reaction ignored when comparing against DMS benchmarks

[b] Multi-electronic-surface rate enhancement factor $\eta = 16/3$ for O_2 -dissociation is not applied when comparing against DMS (MMT-benchmark), but is included in full model (MMT) intended for realistic conditions.

crosses, with corresponding DMS-derived QSS-dissociation-regime values plotted in red. Modified Arrhenius fits to the QCT data (evaluated with Eq. (13) and parameters from Table 3) are shown as continuous black lines. For the dissociation-type reactions shown in Figs. 2(a)-2(h) and 2(j)-2(k) the MMT model is used to evaluate the rate coefficient. Thus, the second dash-dotted red line, labeled “ $f_k^{\text{NB}} = 0.5$ ”, shows the result of evaluating $k_{\text{diss}}^{\text{MMT-NB}}(T, T_v = T)$ (i.e. Eq. (12)) with this particular non-Boltzmann factor. Although the ratio $k_{\text{DMS}}/k_{\text{QCT}}$ does not exactly equal 0.5 for every one of these reactions at every temperature point, Figs. 2(a)-2(h) and 2(j)-2(k) show that this chosen non-Boltzmann factor represents a simple and reasonably accurate approximation common to many reactions and remains valid over a wide temperature range.

For the three exchange-type reactions shown in Figs. 2(l)-2(n) (reactions 16-18 in Table 2) the rate coefficient is evaluated simply with the single-temperature modified Arrhenius form. Our preceding DMS studies in Ref. [23] confirmed that these reactions exhibit only weak, if any, vibrational bias and proceed at near-thermal rates regardless of whether the gas mixture as a whole is in thermal equilibrium, or not.

Reactions 13 and 19-21 in Table 2 do not exhibit constant non-Boltzmann reduction factors, nor do they precisely follow thermal behavior either. This “mixed” behavior becomes even more apparent when the vibrational energy change per reaction of the multiple diatomic species participating in these reactions is examined in Sec. II.D. For model simplicity, for all these reactions, a *thermal* rate coefficient will be used in the CFD model and non-preferential vibrational energy-chemistry coupling will be assumed.

D. Vibrational energy-chemistry coupling terms in MMT model

In addition to nonequilibrium reaction rate coefficients, the two-temperature model must accurately describe vibrational energy-chemistry coupling. These effects are accounted for in the source term:

$$Q_v^{\text{chem}} = \sum_{s \in D} \sum_{r \in R} \left(k_r^f \prod_{q \in S} \left(\frac{\rho_q}{M_q} \right)^{v'_{q,r}} - k_r^b \prod_{q \in S} \left(\frac{\rho_q}{M_q} \right)^{v''_{q,r}} \right) (v''_{s,r} - v'_{s,r}) \langle \varepsilon_{v,s} \rangle_r \quad (18)$$

on the right hand side of Eq. (4). As seen in Eq. (18), the model must supply values for $\langle \varepsilon_{v,s} \rangle_r$, i.e. the average vibrational energy of diatomic species $s \in D$ removed from, or gained by the gas in reaction $r \in R$ as a function of the local translational and/or vibrational temperatures.

Modeling the $\langle \varepsilon_{v,s} \rangle_r$ term in a general fashion is not trivial, because the two main reaction types (dissociation, exchange) exhibit different degrees of vibrational energy-chemistry coupling. In previous work [23] we have found that for the exchange processes vibrational energy removed/replenished per reaction roughly matches that of the diatomic species’ local average in the gas, i.e:

$$\langle \varepsilon_{v,s} \rangle_r^{\text{non-pref.}} = e_{v,s}(T_v)/M_s \quad (19)$$

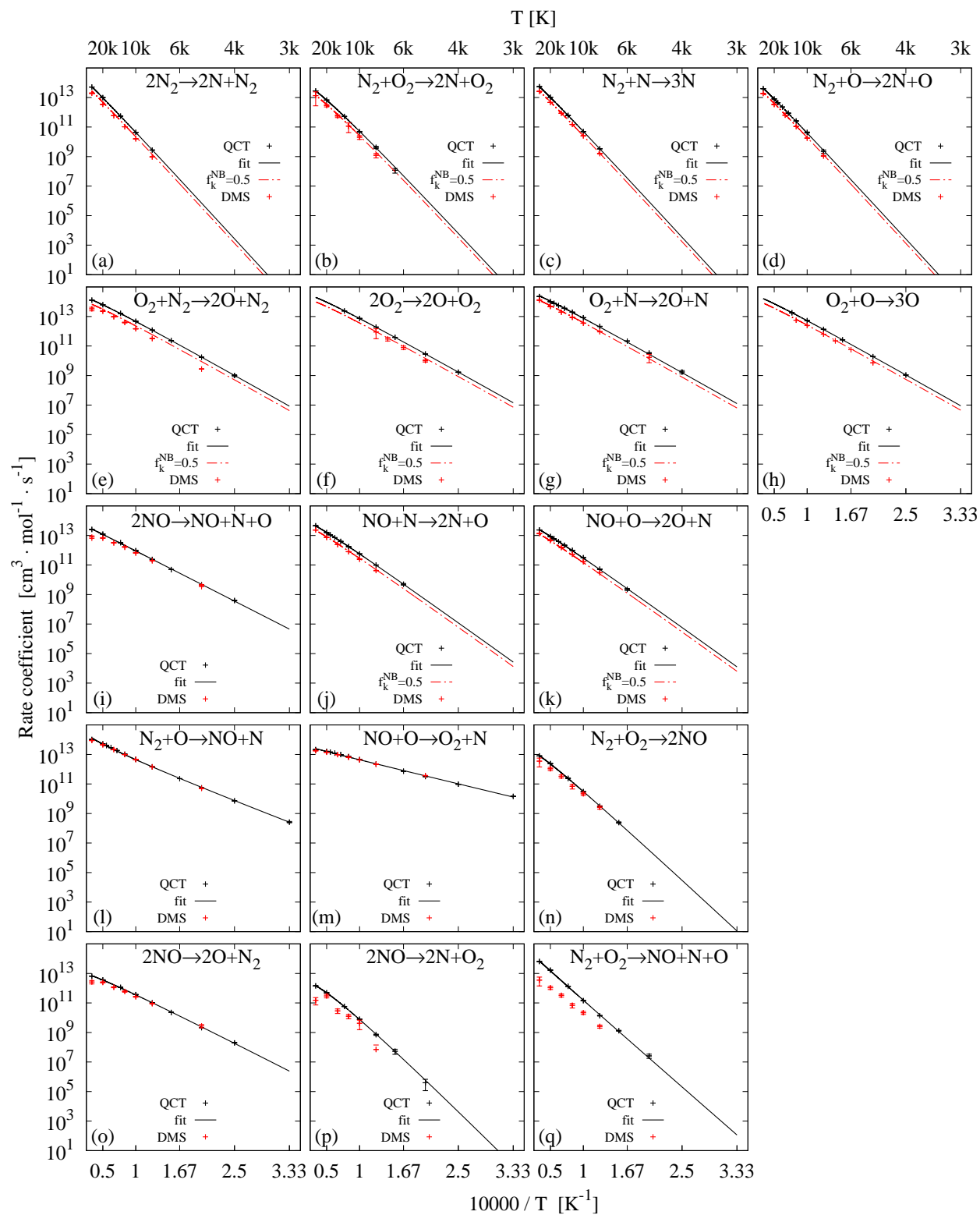


Fig. 2 QCT-derived thermal rate coefficients (black symbols) with Arrhenius fits (black lines) for reactions in Table 2. DMS-derived QSS rate coefficients (red symbols) with Arrhenius fit re-scaled by f_k^{NB} (dash-dotted red lines).

We refer to this as “non-preferential” vibrational energy-chemistry coupling. However, it is also known that this assumption is not well suited for dissociation reactions, which exhibit greater-than-thermal-average, or “preferential” removal of vibrational energy per reaction. Several forms for $\langle \varepsilon_{v,s} \rangle_{\text{diss}}$ have been proposed over the years, in particular for use together with Park’s reaction rates. In an early publication [38] the functional form $\langle \varepsilon_{v,s} \rangle_{\text{diss}} = R (T_{D,s} - T_{t-r})$ was proposed, where $T_{D,s}$ is the dissociation temperature of the species in question. This formulation partially takes into account the local thermodynamic state of the gas through the translation-rotational temperature, but ignores the vibrational energy of the dissociating species. Sharma et al [39] proposed an even simpler expression $\langle \varepsilon_{v,s} \rangle_{\text{diss}} = 0.3 RT_{D,s}$, which does not take into account the local thermodynamic state of the gas at all. Neither of these functional forms reproduce the preferential vibrational energy-chemistry coupling of dissociation observed in our QCT/DMS studies [23].

One major advantage of the MMT model is that it includes an analytical expression for $\langle \varepsilon_{v,s} \rangle_{\text{diss}}$ as a function of the local nonequilibrium thermodynamic state together with the characteristic temperatures $\Theta_{v,s}$ and $T_{D,s}$ of the dissociating species:

$$\langle \varepsilon_{v,s} \rangle_r^{\text{MMT-NB}} = f_{\varepsilon}^{\text{NB}} \left(\frac{k_B \Theta_{v,s}}{\exp(\Theta_{v,s}/T_F) - 1} - \frac{k_B T_{D,s}}{\exp(T_{D,s}/T_F) - 1} \right) \quad (20)$$

As discussed in Sec. II.B of Ref. [14], reaction-specific fit parameters a_U and U^* necessary to compute $\langle \varepsilon_{v,s} \rangle_{\text{diss}}(T_{t-r}, T_v)$ can be extracted from QCT-derived estimates of the same quantity at thermal equilibrium (i.e. when $T_{t-r} = T_v$). Furthermore, Eq. (20) contains another non-Boltzmann correction factor $f_{\varepsilon}^{\text{NB}}$, which was introduced to account for the reduction in vibrational energy removed during the QSS dissociation phase. As will be shown next, this simple correction factor can be calibrated to reproduce $\langle \varepsilon_{v,s} \rangle_{\text{diss}}$ observed in DMS calculations for N_2 , O_2 and NO dissociation [23] with a range of collision partners.

Figure 3 provides an overview of $\langle \Delta \varepsilon_s^v \rangle_r = (v''_{s,r} - v'_{s,r}) \langle \varepsilon_{v,s} \rangle_r$ for all reactions. Here we explicitly plot the net energy *change* per reaction, which will be negative for species being consumed, but positive for species being produced in a given reaction written in the forward sense (recall Eq. (6)). For every reaction, the original thermal-equilibrium QCT data (see Table 2 for sources) are plotted using crosses (red for N_2 , dark blue for O_2 and dark green for NO), with error bars representing the one-standard-deviation error. The corresponding DMS data at the same translational temperature, but extracted during the QSS-dissociation regime, are plotted in orange for N_2 , light blue for O_2 and light green for NO .

The nitrogen and oxygen dissociation reactions in Figs. 3(a)-3(h), as well as the ones involving nitric oxide in Figs. 3(j)-3(k) all rely on Eq. (20) to calculate the vibrational energy change per reaction. For these reactions the solid lines represent $\langle \Delta \varepsilon_s^v \rangle_r = -\langle \varepsilon_{v,s} \rangle_{\text{diss}}^{\text{MMT-NB}}(T, T_v = T)$ of dissociating species $s = \text{N}_2, \text{O}_2$ or NO respectively, evaluated according to Eq. (20) together with the parameters from Table 3, but with $f_{\varepsilon}^{\text{NB}} = 1$. Dash-dotted lines in the same sub-figures represent adjusted curves for $\langle \Delta \varepsilon_s^v \rangle_{\text{diss}} = -\langle \varepsilon_{v,s} \rangle_{\text{diss}}^{\text{MMT-NB}}$ evaluated according to Eq. (20) with a

non-Boltzmann-factor $f_{\epsilon}^{\text{NB}} = 0.85$. Note that, even though the calibration of f_{ϵ}^{NB} in Sec. V of Ref. [14] only involved nitrogen and oxygen dissociation in N_2/N and O_2/O systems, the same non-Boltzmann correction factor also turns out to be a reasonable estimate for several of the other dissociation reactions.

The remaining reactions (reactions 11-13 and 16-21 in Table 2) exhibit either fully thermal, or “mixed” behavior in terms of non-Boltzmann QSS vs. non-preferential trends. As discussed in detail in Ref. [23], rather than decreasing with T , the average vibrational energy removed, or gained in most of these reactions tends to increase with translational temperature, which is more in line with the non-preferential energy coupling assumption discussed in Sec. II.A of Ref. [14]. The clearest examples of this behavior are the two exchange reactions shown in Figs. 3(l) and 3(m) respectively. For the first Zeldovich reaction it can be seen that the QCT- and DMS-predicted values for nitrogen (red and orange symbols in Fig. 3(l) respectively) and nitric oxide (dark and light green symbols) largely follow the same temperature trend as that of the respective average vibrational energy in the gas, i.e. $\langle \Delta \epsilon_{\text{N}_2}^{\text{v}} \rangle_{\text{exch}} \approx -e_{\text{v},\text{N}_2}(T)/M_{\text{N}_2}$ (red dotted line) and $\langle \Delta \epsilon_{\text{NO}}^{\text{v}} \rangle_{\text{exch}} \approx e_{\text{v},\text{NO}}(T)/M_{\text{NO}}$ (dark green dotted line). Recall that, since N_2 is being consumed, $\langle \Delta \epsilon_{\text{N}_2}^{\text{v}} \rangle_{\text{exch}}$ is negative, whereas $\langle \Delta \epsilon_{\text{NO}}^{\text{v}} \rangle_{\text{exch}}$ is positive for the nitric oxide being produced. Although there remains a small gap between the QCT and DMS-predicted values for $\langle \Delta \epsilon_{\text{N}_2}^{\text{v}} \rangle_{\text{exch}}$ and that of $-e_{\text{v},\text{N}_2}(T)/M_{\text{N}_2}$, this non-preferential coupling assumption provides a much better fit than if one had attempted to fit the data to Eq. (20). A similar observation can be made for the second Zeldovich reaction, which involves NO and O_2 instead.

For the remaining reactions in Fig. 3, non-preferential vibration-chemistry coupling seems to fit the QCT/DMS data reasonably well in some species, whereas for other species in the same reaction vibration-preferential “dissociation-type” coupling seems to be a better assumption. Take for instance the mixed dissociation-exchange type reaction (reaction 22 in Table 2) shown in Fig. 3(q). All three diatomic species are involved and the DMS/QCT results suggest that the average vibrational energy of NO molecules being produced is roughly equal to its average vibrational energy in the gas at temperature T (light and dark green symbols vs. dark green dotted line). Thus, non-preferential coupling seems to be the better fit for nitric oxide in this reaction. On the other hand, the two reactant diatomic species exhibit opposing temperature trends. The DMS/QCT data for O_2 (light and dark blue symbols in Fig. 3(q)) show average vibrational energy removed per reaction to be largest at the lowest temperatures and then gradually decreasing at higher T . Thus, $\langle \Delta \epsilon_{\text{O}_2}^{\text{v}} \rangle_{\text{R22}}$ runs opposite to the trend for the thermal average $-e_{\text{v},\text{O}_2}(T)/M_{\text{O}_2}$ (dotted blue line) and oxygen seems to align more with the vibration-preferential coupling behavior observed for dissociation-type reactions. Finally, the DMS/QCT data for nitrogen (orange/red symbols in Fig. 3(q)) show average vibrational energy of N_2 consumed per reaction increasing with temperature T , but at a magnitude noticeably greater than the average present in the gas at temperature T (dotted red line). Thus, describing the behavior of all three species with a vibrationally-favored formulation does not make sense for this reaction. Therefore, in order to avoid over-complicating the model, the choice is made to assume non-preferential vibrational energy-chemistry coupling for all diatomic species participating in any of these reactions (see comment in Table 3).

Table 3 Arrhenius and MMT parameters for QCT-derived reactions

Type	Reaction	C_f [$\frac{\text{cm}^3}{\text{mol}\cdot\text{s}\cdot\text{K}^\eta}$]	η [-]	E_a/k_B [K]	a_U [-]	U^* [K]	Θ_v [K]	note	
1	diss	$2\text{N}_2 \rightleftharpoons 2\text{N} + \text{N}_2$	$1.5259e + 17$	-0.40654	113200	0.49725	265482	3414	
2	diss	$\text{N}_2 + \text{O}_2 \rightleftharpoons 2\text{N} + \text{O}_2$	$1.6671e + 20$	-1.1484	113200	0.36900	376750	3414	
3	diss	$\text{N}_2 + \text{NO} \rightleftharpoons 2\text{N} + \text{NO}$	— Re-use parameters for $2\text{N}_2 \rightleftharpoons 2\text{N} + \text{N}_2$ —						[a]
4	diss	$\text{N}_2 + \text{N} \rightleftharpoons 2\text{N} + \text{N}$	$4.6825e + 17$	-0.51270	113200	0.39547	805087	3414	
5	diss	$\text{N}_2 + \text{O} \rightleftharpoons 2\text{N} + \text{O}$	$3.4678e + 17$	-0.50732	113200	0.35075	-720429	3414	
6	diss	$\text{O}_2 + \text{N}_2 \rightleftharpoons 2\text{O} + \text{N}_2$	$2.3279e + 17$	-0.53233	59330	0.71386	-107879	2251	[b]
			$1.2415e + 18$					$\times 16/3$	
7	diss	$2\text{O}_2 \rightleftharpoons 2\text{O} + \text{O}_2$	$6.4741e + 17$	-0.59391	59330	0.46110	54974	2251	[b]
			$3.4529e + 18$					$\times 16/3$	
8	diss	$\text{O}_2 + \text{NO} \rightleftharpoons 2\text{O} + \text{NO}$	— Re-use parameters for $2\text{O}_2 \rightleftharpoons 2\text{O} + \text{O}_2$ —						[a]
9	diss	$\text{O}_2 + \text{N} \rightleftharpoons 2\text{O} + \text{N}$	$1.7446e + 17$	-0.44587	59330	0.37965	-313988	2251	[b]
			$9.3045e + 17$					$\times 16/3$	
10	diss	$\text{O}_2 + \text{O} \rightleftharpoons 3\text{O}$	$1.5537e + 17$	-0.47445	59330	0.36157	96143	2251	[b]
			$8.2864e + 17$					$\times 16/3$	
11	diss	$\text{NO} + \text{N}_2 \rightleftharpoons \text{N} + \text{O} + \text{N}_2$	— Re-use parameters for $2\text{NO} \rightleftharpoons \text{N} + \text{O} + \text{NO}$ —						[a]
12	diss	$\text{NO} + \text{O}_2 \rightleftharpoons \text{N} + \text{O} + \text{O}_2$	— Re-use parameters for $2\text{NO} \rightleftharpoons \text{N} + \text{O} + \text{NO}$ —						[a]
13	diss	$2\text{NO} \rightleftharpoons \text{N} + \text{O} + \text{NO}$	$3.5889e + 14$	-0.07945	52644	-Treat as non-preferential-			
14	diss	$\text{NO} + \text{N} \rightleftharpoons 2\text{N} + \text{O}$	$2.5759e + 17$	-0.59741	75360	0.51679	3876179	2744	
15	diss	$\text{NO} + \text{O} \rightleftharpoons \text{N} + 2\text{O}$	$7.0310e + 16$	-0.52778	75360	0.30100	-3007416	2744	
16	exch	$\text{N}_2 + \text{O} \rightleftharpoons \text{NO} + \text{N}$	$1.6339e + 11$	0.76972	37850	-Treat as non-preferential-			
17	exch	$\text{NO} + \text{O} \rightleftharpoons \text{O}_2 + \text{N}$	$1.99183e + 13$	0.10007	24427	-Treat as non-preferential-			
18	exch	$\text{N}_2 + \text{O}_2 \rightleftharpoons 2\text{NO}$	$1.15292e + 18$	-0.83459	97485	-Treat as non-preferential-			
19	mixed	$2\text{NO} \rightleftharpoons 2\text{O} + \text{N}_2$	$1.1786e + 16$	-0.54728	53783	-Treat as non-preferential-			
21	mixed	$2\text{NO} \rightleftharpoons 2\text{N} + \text{O}_2$	$1.3688e + 21$	-1.6611	106199	-Treat as non-preferential-			
22	mixed	$\text{N}_2 + \text{O}_2 \rightleftharpoons \text{NO} + \text{N} + \text{O}$	$2.9053e + 14$	0.15022	89282	-Treat as non-preferential-			

[a] Reaction ignored when comparing against DMS

[b] Ground-electronic-state values for C_f , used when comparing against DMS. Multiplied by multi-electronic-surface rate enhancement factor of 16/3 for O_2 -dissociation (see row below)

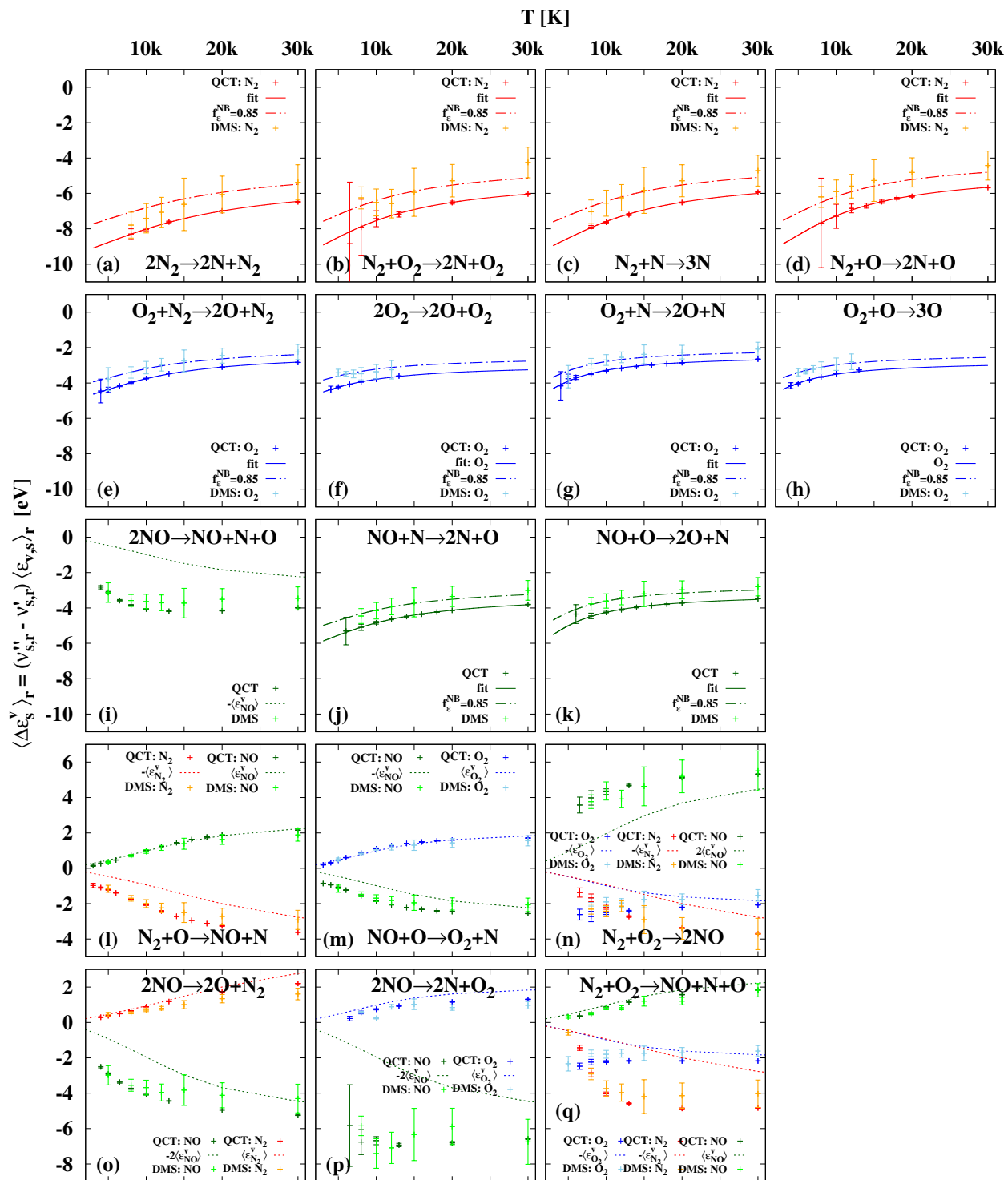


Fig. 3 Average vibrational energy changes of diatomic species N₂ (red), O₂ (blue) and NO (green) per reaction.

III. MMT model comparison against Direct Molecular Simulations

In Sec. III of Ref. [14], we presented a first set of comparison calculations for our CFD implementation of the MMT model against DMS benchmark solutions. Those calculations dealt exclusively with “pure” N_2/N and O_2/O mixtures and thus only involved dissociation reactions of the respective diatomic species. In this section we extend this effort to the full MMT model for 5-species air (i.e. N_2 , O_2 , NO , N and O), which now includes formation and consumption of nitric oxide via the Zeldovich exchange reactions, among others. Thus, we now employ the more complete set of curve-fit parameters required to evaluate Landau-Teller type vibrational relaxation times from Sec. II.B and the kinetic rate parameters from Sec. II.C in this paper. As mentioned in Sec. III of Ref. [14], such CFD comparisons must be performed consistently by including only collision-pair interactions corresponding to the available PESs used in the DMS calculations. This also means that the thermodynamic properties employed in the CFD-MMT calculations of this section explicitly *do not* account for contributions of molecular or atomic species’ electronic excited states. Refer to Tables 1 and 3 (including footnotes) for the interactions modeled and parameters used for MMT results presented in this section. Further recall that constant non-Boltzmann factors of $f_k^{NB} = 0.5$ and $f_\varepsilon^{NB} = 0.85$ are employed in Eq. (12) and (20) respectively throughout all MMT calculations presented in this section.

A. Vibrational excitation and dissociation of 5-species air mixture in isothermal heat baths

In analogous fashion to Ref. [14], the first set of comparison calculations are carried out in isochoric, isothermal heat baths. In the CFD calculations we keep the mixture trans-rotational temperature fixed over time, while the mixture vibrational temperature is initially set to 300 K and the initial number density to 10^{24} m^{-3} . The gas now consists of a molecular nitrogen/oxygen mixture with initial mole fractions $x_{N_2} = 0.8$ and $x_{O_2} = 0.2$ respectively. As was the case in Sec. VII.A of Ref. [14], the initial conditions are slightly different for the DMS reference calculations. Here, every species’ respective translational temperature is kept constant by re-sampling their center-of-mass velocities from their respective Maxwellians at the heat bath’s temperature after every time step. Meanwhile, the internal energy states of all molecules initially present are sampled from the respective Boltzmann rovibrational distribution at common $T_{r,N_2}(t=0) = T_{v,N_2}(t=0) = 300 \text{ K}$ and $T_{r,O_2}(t=0) = T_{v,O_2}(t=0) = 300 \text{ K}$ respectively. Thus unlike the CFD calculations, where translational and rotational modes are assumed to be equilibrated at all times, in the DMS calculation there exists an additional early phase of rotational nonequilibrium. Beyond N_2 - and O_2 - dissociation responsible for the formation of atomic nitrogen and oxygen, these test cases simulate the production of nitric oxide, primarily as a result of the Zeldovich exchange reactions. In addition to this, a range of other reactions involving NO molecules affect the overall evolution of the 5-species mixture composition.

In Figs. 4a-4d we compare predictions with the CFD-MMT model to DMS reference solutions at $T = 8000 \text{ K}$ - 20000 K respectively. All figures follow the pattern established in Sec. VII.A of Ref. [14], with time-dependent vibrational and rotational temperatures plotted in the upper half and corresponding species mole fraction profiles in

the lower half. As before, CFD-MMT profiles are plotted with dash-dotted lines and corresponding DMS results with continuous ones of the same color. Some of the DMS solutions used for reference were originally presented in Ref. [23] and additional details may be found therein.

Note that both for the CFD-MMT and DMS calculations the temperature profiles shown represent mixture-weighted values. Since these air mixtures may contain up to three diatomic species simultaneously, in the CFD-MMT calculations the mixture vibrational temperature T_v at every time step is calculated as implicit solution to the equation:

$$E_v = \sum_{s \in D} \rho_s e_{v,s}(T_v) \quad (21)$$

where the instantaneous mixture vibrational energy per unit volume $E_v = \rho e_v$ is one of the state variables in the governing equations (see Eq. (5) in Ref. [14]) and each diatom's specific vibrational energy is calculated from Eq. (S20) in the supplemental information. As discussed there, for these comparisons against DMS we employ the custom PES-derived Lewis-fit type parameters from Table S2 to evaluate $h_s^{\text{Lewis-fit}}$ in Eq. (S20) of the supplemental information. Therefore, we deliberately exclude electronic excited state contributions of any of the 5 species.

For the $T = 8\,000$ K-case the upper half of Fig. 4a shows that the CFD model does an excellent job of replicating the vibrational excitation behavior predicted by DMS (dash-dotted red vs. solid T_v lines). Thus, the assumption of constant T_{t-r} inherent in the two-temperature CFD model is satisfied for practically the entire simulated time. Furthermore, just as was observed in Sec. VII.A of Ref. [14], in Fig. 4a we see that both the CFD- and DMS-derived vibrational temperature profiles level off at a value slightly below T and do not fully equilibrate with the heat bath temperature for the remainder of simulated time. Thus, as was seen for the simpler N_2/N and O_2/O mixtures, the DMS reference calculations for 5-species air point to the existence of a QSS-dissociation phase responsible for this temperature gap. Note that, as discussed in Ref. [23], the presence of additional reactions in 5-species air (e.g. Zeldovich exchange and other reactions) does not prevent this QSS dissociation phase from being established.

In the lower half of Fig. 4a we compare mole fraction profiles for all 5 species (N_2 in red, O_2 in dark blue, NO in green, N in orange and O in light blue) and observe very close agreement between CFD (dash-dotted lines) and DMS (solid lines) results. The CFD-MMT results reproduce all major features of the reference calculations, such as the early drop in molecular oxygen from $x_{O_2} = 0.2$ to nearly zero (primarily due to rapid $O_2 - O_2$, $O_2 - N_2$ and $O_2 - O$ dissociation), the early decrease from $x_{N_2} = 0.8$ to about 0.65 and near-simultaneous rise in nitric oxide mole fraction from zero to its peak of $x_{NO} \approx 0.18$ (both caused by the first Zeldovich reaction $N_2 + O \rightarrow NO + N$). Beyond this point CFD-MMT closely matches DMS in predicting the subsequent slow decline in x_{N_2} and x_{NO} due to dissociation, accompanied by a simultaneous rise in atomic nitrogen and oxygen mole fractions. The only notable discrepancy is a small time lag building up at later times between the CFD- and DMS-derived x_{N_2} -profiles in red, mirrored by the corresponding x_N -profiles in orange. However, these relative discrepancies in mixture composition never exceed a few

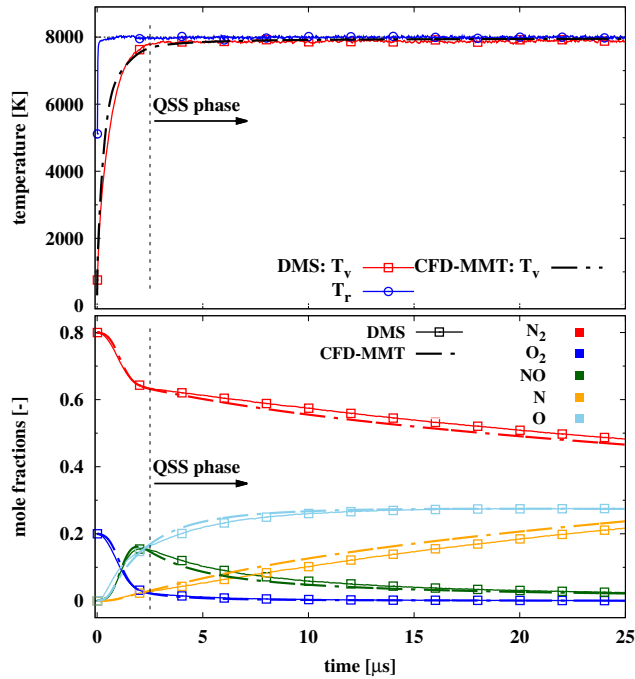
percent.

In Figs. 4b-4d we compare CFD-MMT and DMS predictions for the same 5-species air mixture, but at increasingly higher the heat bath temperatures. Overall agreement between both methods' predicted T_v profiles (dash-dotted vs. continuous red lines) is good, despite stronger coupling between vibrational and rotational modes in the DMS results. This effect is particularly noticeable for cases $T = 15\,000\text{ K}$ and $20\,000\text{ K}$ where the DMS calculations predict that rotational and translational modes remain slightly out of equilibrium for the duration of the QSS phase. Furthermore, mixture composition profiles in Figs. 4b-4d reveal that, with increasing T a greater portion of chemical activity takes place before the gas even enters the QSS dissociation regime. Differences between predicted mixture compositions are most noticeable early on, during the vibrational (and rotational in DMS) excitation phase. Recall that in the two-temperature CFD model a common translation-rotational temperature $T_{t-r} = T_t = T_r$ is being imposed. Separate rotational relaxation is not modeled in CFD and any rotation-vibration coupling is ignored. Since the rotational mode starts out fully excited at $t = 0$, the initial gas in the CFD calculation possesses a higher enthalpy than in the DMS solution. This allows for faster initial dissociation of O_2 , in turn causing faster production of atomic oxygen and subsequent faster N_2 -consumption coupled with faster NO-formation through the first Zeldovich reaction. Despite these built-in simplifications the CFD model does a remarkably good job of reproducing all major features of the DMS reference solutions at this higher temperature.

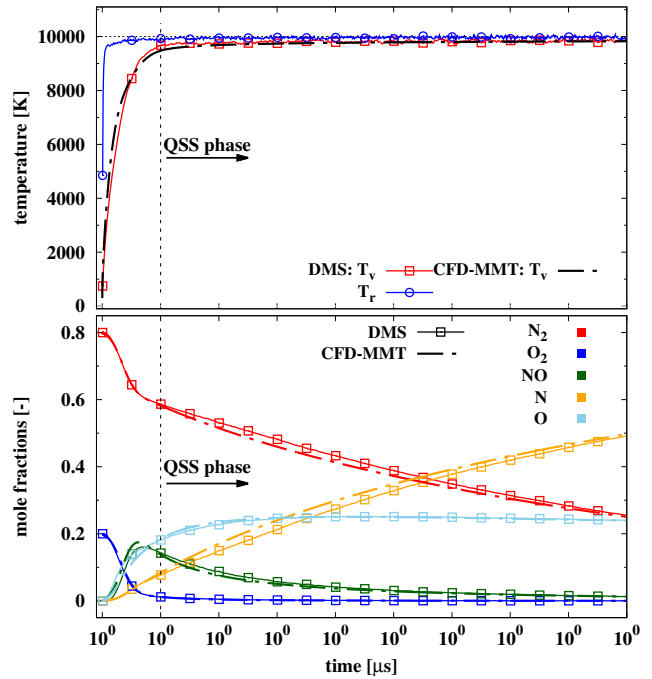
B. Vibrational excitation and dissociation of 5-species air mixture in adiabatic heat baths

After the isothermal heat bath comparisons of Sec. III.A, we perform a similar analysis for adiabatic conditions. In this scenario the heat bath's total energy remains constant and translational temperature freely adjusts in response to internal energy redistribution processes and chemical reactions, which gradually drive the gas closer to equilibrium. These conditions allow us to better assess the MMT model's behavior over a wide temperature range within a single calculation and it is more representative of post-shock conditions.

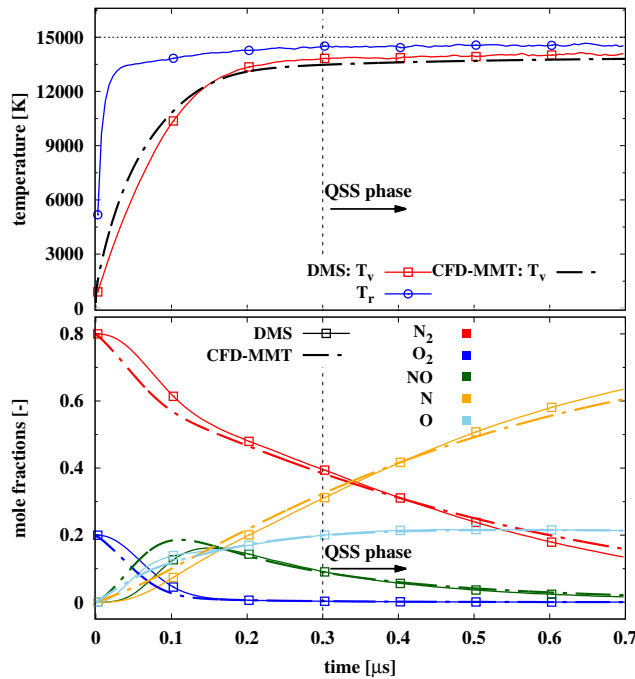
Two separate cases for 5-species air are simulated using the MMT model and compared to corresponding DMS reference solutions. Both cases are distinguished by their heat bath's respective specific enthalpy (constant throughout the simulation). Initial conditions are summarized in Table 4 and, as was the case for the isothermal heat baths of Sec. III.A, they differ slightly between CFD and the equivalent DMS calculations. In the DMS calculations the translational temperature $T_t^{\text{DMS}}(t = 0)$ (same for N_2 and O_2) is initialized at a higher value than the common rotational and vibrational temperatures $T_r^{\text{DMS}}(t = 0) = T_v^{\text{DMS}}(t = 0)$, causing both molecular oxygen and nitrogen to undergo rapid early translation-rotational relaxation, in parallel with a slower vibrational excitation phase. By construction in the two-temperature CFD model, mixture translational and rotational modes remain in equilibrium at all times. Thus, we initialize the combined translation-rotational temperature to the weighted average $T_{t-r}^{\text{CFD}}(t = 0) = \frac{3}{5}T_t^{\text{DMS}}(t = 0) + \frac{2}{5}T_r^{\text{DMS}}(t = 0)$ in order to match the enthalpy of the DMS case. Recall that the weights $c_v^t/(c_v^t + c_r^t) = 3/5$



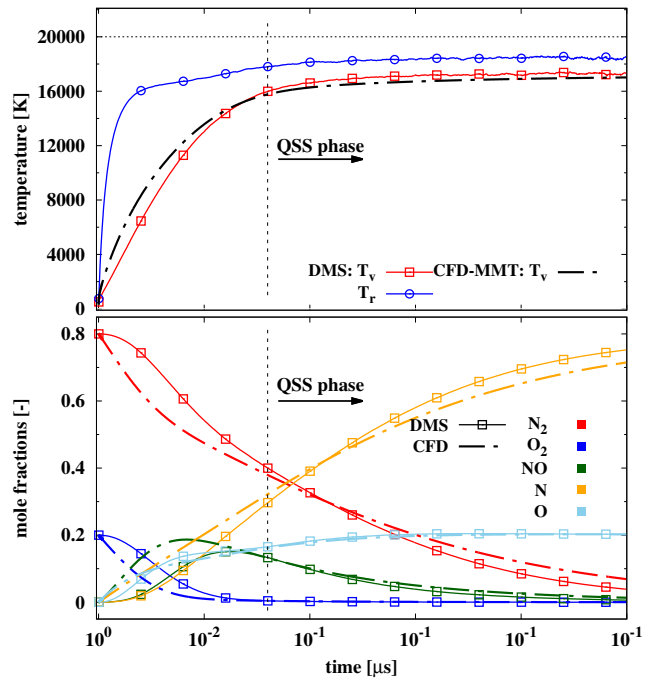
(a) Isothermal heat bath at $T = 8000$ K



(b) Isothermal heat bath at $T = 10000$ K



(c) Isothermal heat bath at $T = 15000$ K



(d) Isothermal heat bath at $T = 20000$ K

Fig. 4 Comparison of CFD-MMT model against DMS: 5-species air in isothermal heat bath

Table 4 DMS and CFD initial conditions for adiabatic heat bath calculations in 5-species air

h	$\rho \times 10^3$	initial moles	DMS initial conditions			CFD initial conditions		
			T_t	$T_r = T_v$	p	T_{t-r}	T_v	p
[MJ/kg]	[kg/m ³]	[-]	[K]	[K]	[kPa]	[K]	[K]	[kPa]
10.1	1.96	80%N ₂ , 20%O ₂	19 900	300	11.3	12 100	300	6.83
17.9	2.52	80%N ₂ , 20%O ₂	36 600	300	26.6	22 100	300	16.1

and $c_v^r/(c_v^t + c_v^r) = 2/5$ correspond to the relative energy contributions to heat capacity at constant volume of the translational and rotational modes in a fully excited diatomic gas. In each one of the six cases the initial translation-rotational temperature of the CFD calculations will be lower than the DMS’s initial translational one, because the two modes in CFD begin “pre-equilibrated”. As seen in Table 4, this also has repercussions for the initial pressures in the CFD and DMS calculations.

Focusing on the lower-enthalpy case first, the upper half Fig. 5a, shows DMS profiles of mixture translational, rotational and vibrational temperature as continuous black, blue and red lines respectively. The mixture rotational and vibrational temperatures are computed in the same manner as in Sec. III.A, taking into account composition-weighted contributions of all three diatomic species. The mixture translational temperature is calculated directly as $T_t^{\text{DMS}} = p/(n k_B)$, where n is the instantaneous mixture number density and the instantaneous mixture static pressure in turn is calculated as the trace of the mixture kinetic pressure tensor $p = \frac{1}{3} (p_{xx} + p_{yy} + p_{zz})$, as defined in App. C of Ref. [22]. A combined mixture trans-rotational temperature for DMS (continuous gray line) is now computed as $T_{t-r}^{\text{DMS}} = 3/5 T_t^{\text{DMS}} + 2/5 T_r^{\text{DMS}}$. Corresponding CFD profiles for mixture trans-rotational and vibrational temperatures (dash-dotted gray and red lines) are shown in the upper half of Fig. 5a. Near-exact overlap between the T_{t-r} -profiles obtained with both methods can be observed, whereas the CFD vibrational temperature runs slightly ahead the DMS counterpart during the initial relaxation phase. However, this temperature gap never exceeds a few percent and narrows toward the end of the simulated time. The bottom half of Fig. 5a shows DMS mole fraction profiles of all five mixture components using the same color scheme and line patterns established in Sec. III.A. Over the course of the first 100 microseconds one observes the initial 20% of O₂ (dark blue lines) being almost completely consumed, while the mole fraction of N₂ decreases from 0.8 to roughly 0.65 in the same time span. The decrease in O₂ mole fraction can be attributed almost exclusively to dissociation (reactions 6-7 and 9-10 in Table 2). On the other hand, the main cause for the early drop in N₂ concentration is the first Zeldovich reaction (reaction 16 of Table 2) rather than N₂-dissociation itself. The exchange reaction activates as soon as the first oxygen atoms become available, producing nitric oxide and atomic nitrogen in the process. Very close agreement between the CFD- and DMS-predicted mole fraction profiles for N₂ (dash-dotted vs. continuous red lines), O₂ (dark blue) and N (orange) can be observed for the entire 100 microseconds plotted. For nitric oxide (dark green lines) and atomic oxygen (light blue) differences become most noticeable in the time window spanning 1 – 50 μ s. During this interval the CFD model predicts simultaneously higher

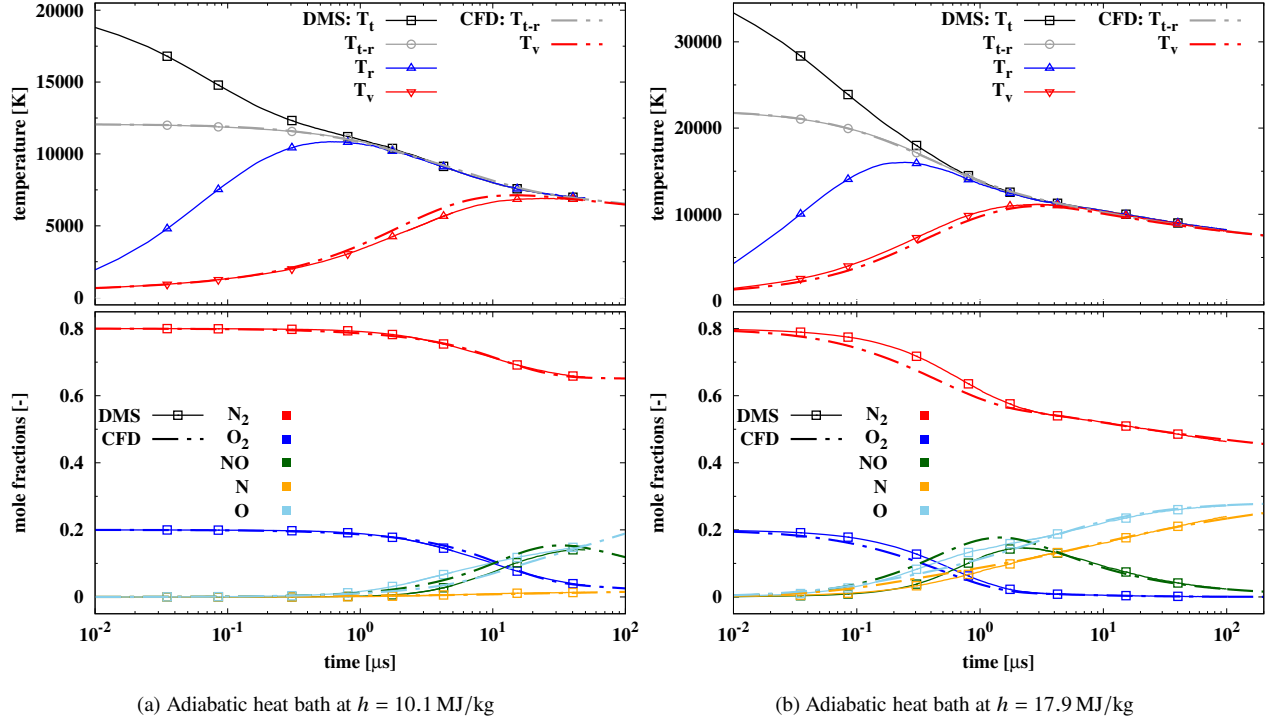


Fig. 5 Comparison of CFD-MMT model against DMS: 5-species air in adiabatic heat bath

NO and lower O mole fractions than the DMS calculation.

Results for the higher-enthalpy case are shown in Fig. 5b. As seen in the upper half of the figure, vibration-translational relaxation is effectively complete after the first 5 microseconds, nearly ten times quicker than at the lower-enthalpy conditions. Again, very close agreement between the CFD-predicted profiles for T_{t-r} and T_v (dashed-dotted gray and red lines) and the equivalent DMS solution (continuous lines) can be observed. These two adiabatic cases further confirm that the MMT model does a remarkably good job of reproducing all major features observed in the benchmark DMS solutions, insofar as this can be expected given the simplifying assumptions of the two-temperature CFD implementation.

IV. MMT model behavior when approaching chemical equilibrium

Section VI of Ref. [14] discusses limitations inherent to the use of constant non-Boltzmann correction factors when evaluating dissociation rate coefficients and associated vibrational energy removed by dissociation in the MMT model (recall Eqs. (12) and (20)). As a remedy, the variable (i.e. composition-dependent) non-Boltzmann factors are introduced, which enable the model to reproduce the correct forward(dissociation)/backward(recombination) rates and vibrational energy removal/replenishment rates as the gas mixture reaches thermo-chemical equilibrium.

In this section we examine the aggregate effect of switching from constant to variable non-Boltzmann factors in actual CFD simulations. Three sets of results, all using the MMT model, are shown in Fig. 6 at the two lower heat

bath temperatures from Sec. III.A. All use the exact same reaction rate and vibrational relaxation parameters as in the model benchmarking calculations of Sec. III.A. The only difference is that the first one employs constant values $f_k^{\text{NB}} = 0.5$ and $f_\varepsilon^{\text{NB}} = 0.85$ and has all recombination reactions disabled (continuous lines, labeled as “NB, no rec.” in Figs. 6a and 6b). Thus, it is identical with the MMT solutions previously presented in Figs. 4a and 4c, but integrated further in time (up to a total of 1 000 microseconds for the lower-temperature case). The much longer integration times in Fig. 6 relative to Fig. 4 become necessary to observe the gas mixture’s eventual approach to chemical equilibrium. The second set (open circles labeled as “NB, with rec.” in Figs. 6a and 6b) uses the same constant factors, but has recombination reactions enabled. Finally, the third set of results (dash-dotted lines labeled as “VNB, with rec.” in Figs. 6a and 6b) employs the variable factors as given by Eq. (28) of Ref. [14] and also has recombination reactions enabled.

Focusing on the lower-temperature case first, Fig. 6a reveals several commonalities. First, during the early stages, when the gas consists primarily of molecular species N_2 and O_2 , all three solutions are identical. This is to be expected, given that during this period the nonequilibrium concentration ratios z_r (Eq. (27) in Ref. [14]) of all major dissociation reactions are close to zero (thus $f_k^{\text{VNB}}(z_r \rightarrow 0) \approx 0.5$ and $f_\varepsilon^{\text{VNB}}(z_r \rightarrow 0) \approx 0.85$) and recombination rates are still negligible. Later on, by the time T_v has almost reached the heat bath temperature and sufficient atomic nitrogen and oxygen have built up in the mixture, differences become more noticeable. In the solution with constant non-Boltzmann factors and recombination disabled, T_v eventually attains its QSS-dissociation-phase value and remains unchanged for the rest of the calculation. Meanwhile, dissociation of N_2 , O_2 and NO continue unopposed until nothing but atomic nitrogen and oxygen remain in the mixture and true thermodynamic equilibrium is never reached. In the two solutions with recombination enabled, T_v also first approaches the QSS-phase plateau, but eventually continues climbing to fully equalize with the heat bath temperature (see close-ups in temperature plots). This occurs in tandem with the species mole fraction profiles leveling off and approaching the thermodynamic equilibrium composition at temperature T and final equilibrium pressure in the heat bath.

Any differences in final mixture composition between the three calculations are most noticeable at this lower-temperature condition, because the respective equilibrium compositions comprise small, but still noticeable amounts of molecular nitrogen. By contrast, at the higher-temperature condition shown in Fig. 6b, true thermodynamic equilibrium compositions are already skewed so far toward the atomic species that any differences in final mole fractions between the three calculations become negligible and the only straightforward way to distinguish them is through the temperature profiles. For this higher-temperature heat bath the gaps between T and T_v during QSS are much more noticeable and all three solutions reach this plateau together. As before, the solution using constant non-Boltzmann factors and neglecting recombination settles in at this QSS value, whereas in the other two solutions recombination reactions end up balancing with dissociation and prevent the entirety of diatoms from disappearing. Vibrational relaxation of this small remaining amount of diatomic species (mostly N_2) ultimately drives T_v toward

equilibrium with the heat bath temperature.

At both conditions examined, the two solutions that include recombination reactions, regardless of whether they employ constant or variable non-Boltzmann factors (unfilled circles vs. dashed lines), exhibit nearly identical behavior. Indeed, any differences are so small that they become almost indistinguishable at the scale of the plots. Thus, paradoxically the use of the arguably more accurate variable non-Boltzmann factors does not alter the overall results significantly. This apparent contradiction has a rather simple explanation: As discussed in Sec. VI of Ref. [14], the whole point of making the non-Boltzmann factors dependent on nonequilibrium concentration ratio z_r is that this dynamically re-scales dissociation and recombination rate coefficients (and related vibrational energy removal/replenishment rates) so that each, on their own, attain their expected *thermal* rates as the mixture approaches equilibrium. By construction, when $z_r \rightarrow 1$ close to the mixture's chemical equilibrium composition, differences between reaction rates computed using constant vs. variable non-Boltzmann factors are greatest. However, these differences are only evident when comparing one-way forward or backward rates. The *net* rates of reaction and vibrational energy removal (e.g. Eqs.(25) and (26) in Ref. [14]) on the other hand, are barely affected by this difference, since the same factors (constant or variable) are applied simultaneously to the forward and backward contributions to these terms.

In summary, the result of the comparisons in Fig. 6 is that at low- and high-temperature conditions the main distinguishing factor between the three sets of calculations is not whether constant or variable non-Boltzmann factors were used, but rather whether recombination reactions were included or neglected. Despite this, we recommend the MMT model to always be used with recombination enabled and to employ variable non-Boltzmann factors.

V. Final additions to internal energy and MMT models

In Sec. III we compared the MMT model for 5-species air against benchmark solutions and all efforts concentrated on ensuring a consistent CFD vs. DMS comparison. It meant employing a set of model parameters that accounted for the limitations inherent to the DMS reference solutions. However, MMT is ultimately intended for studying real-world high-temperature flows generated in ground test facilities, or for simulating actual hypersonic flight conditions, which involves completing several components of the model.

First, we add electronic-excited-state energy contributions into the calculation of thermodynamic properties by reverting from the ground-electronic-state-only (PES-derived) curve fits to the original NASA Lewis ones (see discussion in Sec. S1.A of the supplemental information). This implies a shift from viewing T_v as a purely vibrational temperature to one representing the energy content of a combined vibrational-electronic mode. It also implies that, by construction, vibrational and electronic energy relaxation rates will now be tightly coupled. As described in Sec. II.B, we also modify the manner in which we calculate the pair-wise vibrational relaxation times. We switch from the slower τ^v -parameters for some of the relaxation pairs (marked with an asterisk superscript in Table 1) to the faster ones (marked with a double-asterisk superscript). Furthermore, we replace the parameters yielding near-infinite relaxation

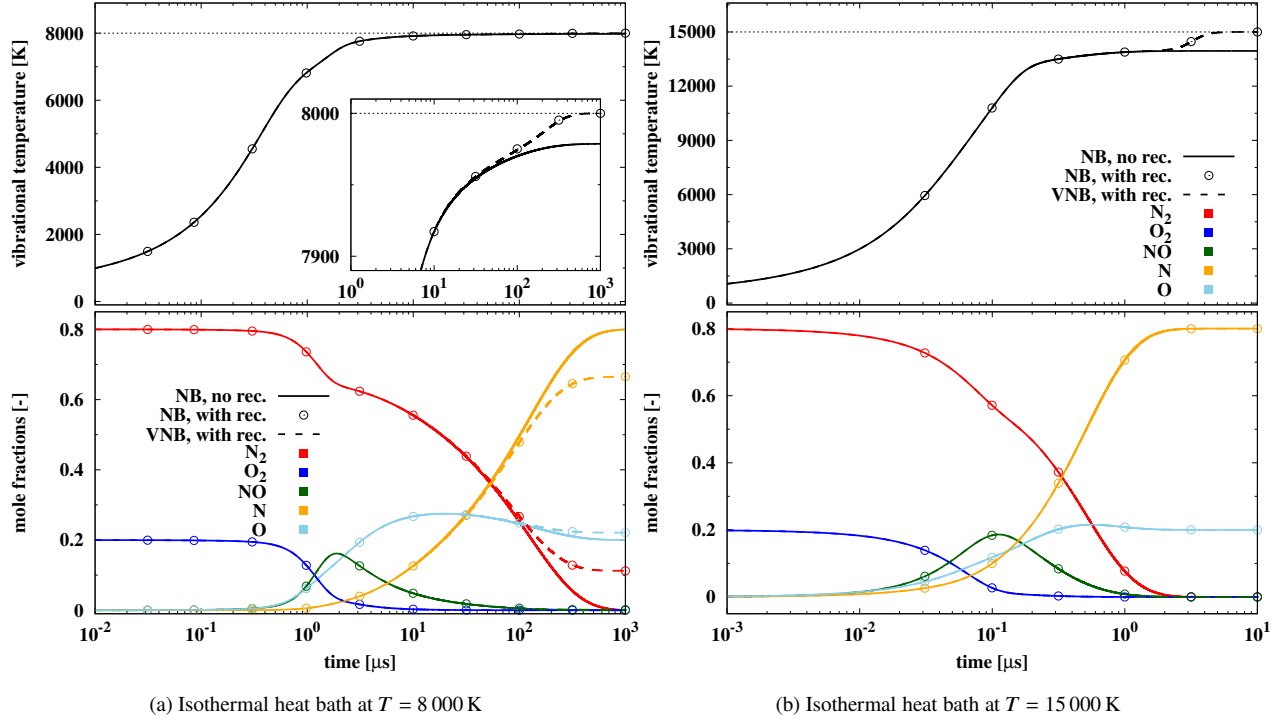


Fig. 6 Isothermal heat bath: MMT solutions obtained using constant (NB) vs. variable (VNB) non-Boltzmann factors

Table 5 Choice of MMT model parameters used to simulate model-benchmarking-only vs. complete air mixtures

	MMT-benchmark	MMT (no η_{O_2} factor)	MMT (full η_{O_2} factor)
thermodynamics fits	PES-derived	NASA Lewis	NASA Lewis
vibrational relaxation	parameter set [*]	parameter set [**]	parameter set [**]
kinetic rate data	17 reactions	21 reactions	21 reactions
multi-surface factor: η_{O_2}	no	no	applied to reactions 6-10 in Table 3

times for NO – N₂, NO – O₂, N₂ – NO and O₂ – NO with available parameters of what we consider the most similar interaction pairs (see Table 1). We now also include all reactions absent from the “benchmarking” set (see footnote [a] in Tables 2 and 3), again by using data from what we consider the most similar available reactions to act as stand-ins for the unavailable ones. Finally, as mentioned in Sec. II.C.2, it may become necessary to modify the oxygen dissociation rate coefficients to include a multi-surface factor $\eta_{O_2} = 16/3$ (see footnote [b] in Tables 2 and 3 and related discussion in Sec. II.C.2) in order to account for enhanced dissociation rates from electronically excited O₂.

In Table 5 we summarize the aforementioned changes, which result in three distinct versions of the MMT model for 5-species air: the MMT-benchmark version, the MMT version without enhancement factor η_{O_2} and the MMT model with the enhancement factor applied equally to all 5 oxygen dissociation reactions. In the remainder of this section we compare predictions with these three versions against each other to assess the effect that these changes have.

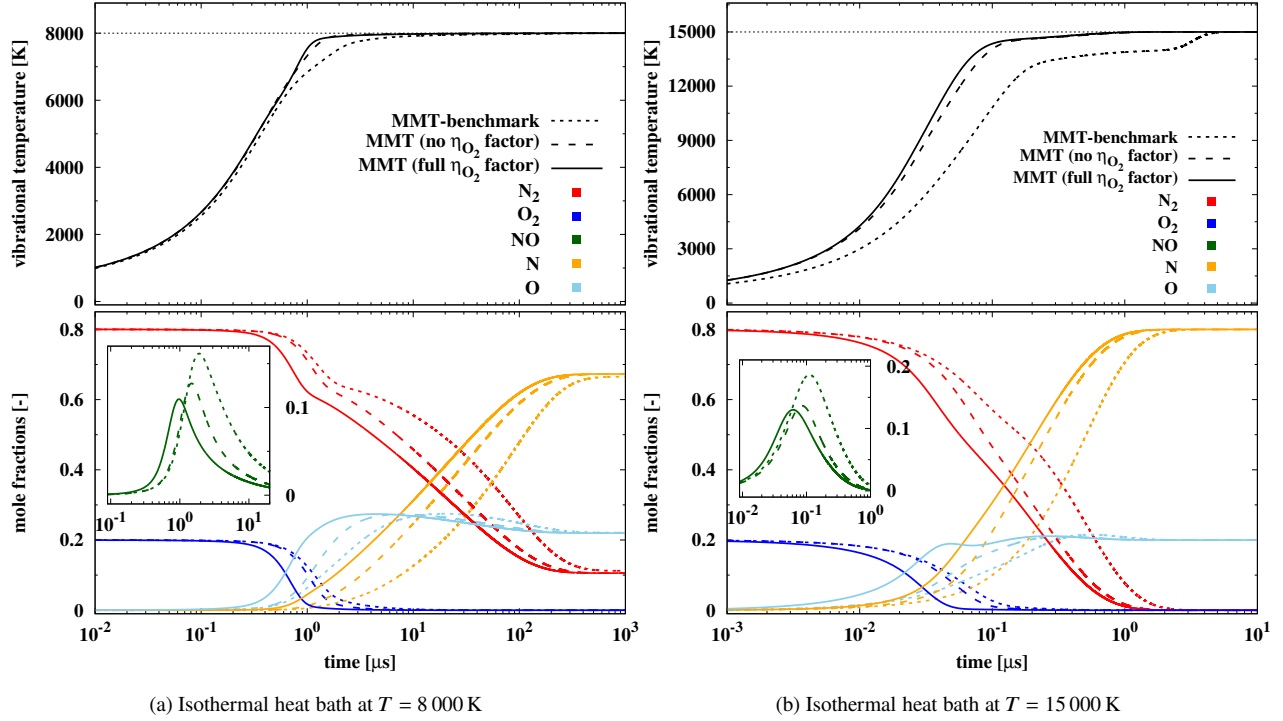


Fig. 7 Isothermal heat bath results for the tree MMT parameter sets of Table 5

In Fig. 7, comparisons are made for heat bath temperatures $T = 8\,000\text{ K}$ and $15\,000\text{ K}$ and three sets of calculations are shown in each sub-figure: the first using the MMT-benchmark parameter set (dotted lines), the second using the MMT parameter set without the multi-surface enhancement factor for oxygen dissociation (dashed lines) and the third applying said factor equally to the 5 oxygen dissociation reactions (reactions 6-10 in Table 3). All three sets of calculations employ the variable non-Boltzmann correction factors discussed in Sec. IV and treat all reactions in Table 3 as reversible. Thus, the MMT-benchmark solutions in Fig. 7 are identical with the “VNB, with rec.” solutions from Sec. IV (dashed lines in Fig. 6).

As expected, the MMT-benchmark results are significantly different compared to the other two solutions, as this parameter set uses slower vibrational relaxation times for some species and is missing internal energy relaxation pairs and reactions for some species. Clear differences seen in Fig. 7 include that the rise in T_v is noticeably slower in the MMT-benchmark result and that the QSS temperature plateau is established at a much lower value, compared to the other two solutions.

The important differences in Fig. 7 to focus on are those between the MMT results with and without the electronic excitation factor. The addition of the multi-surface enhancement factor to the 5 oxygen dissociation reactions has a significant effect in speeding up the rate at which O_2 is removed from the mixture. Any uncertainty in this parameter will thus have a major effect on the predicted overall O_2 consumption and associated O production rate. Furthermore, the rate at which O -atoms become available early on also controls the rate at which the first Zeldovich reaction is able

to begin producing the first NO-molecules. Both figures also highlight the crucial role that the two exchange reactions play in shaping the overall evolution of the mixture composition, as the first Zeldovich reaction is responsible for producing much of the early N atoms, which may then be partially consumed in the second Zeldovich reaction running in its exothermic sense. This further increases the O₂ consumption rate in the process. Beyond this, the first Zeldovich reaction remains the greatest contributor to the net rate of N₂ destruction taking place over the entire simulated time, whereas the effect of the 5 nitrogen dissociation reactions is small by comparison. Although not shown here, these findings are broadly replicated at the higher-temperature heat bath conditions.

VI. Comparison of MMT and Park+M&W models

In this section we compare the MMT model’s predictions against those of the well-established Park TT_v model for high-temperature air [27]. The Park model is usually employed in combination with vibrational relaxation rates from the Millikan and White correlation [28] and Park’s own high-temperature correction [40]. In the Park simulations we include only the reactions listed in Table 2 of Ref. [29] under the heading “Dissociation Reactions” which involve the five neutral air species N₂, O₂, NO, N and O, in addition to the two Zeldovich reactions listed in the same table under the heading “NO Exchange reactions”. The M&W and high-temperature correction parameters are taken from the section entitled “Vibrational Relaxation Parameters”, also in Ref. [29].

For the MMT model in this section we report two separate results using the parameter set either with, or without applying the multi-electronic-surface rate enhancement factor to all oxygen dissociation reactions (see two rightmost columns in Table 5). As a reminder, in the MMT model we evaluate the vibrational energy change per dissociation using Knab’s formula modulated by the variable non-Boltzmann factor (Eqs. (16) and (17) in Ref. [14]) for most dissociation reactions (reactions 1-10 and 14-15 and in Table 2), whereas the remaining reactions assume non-preferential (i.e. $\langle \varepsilon_{v,s} \rangle_r = e_{v,s}(T_v)/M_s$) vibrational energy-chemistry coupling. By contrast, in the Park model simulations we treat the vibrational energy change per reaction as non-preferential for all processes, regardless of whether they represent dissociation, or exchange reactions (see Eq. (9) in Ref. [14]). Finally, note that in both the MMT and Park+M&W simulations we now compute the thermodynamic properties (heat capacities, vibrational-electronic energies, Gibbs free energies) of all five species taking into account the contributions of excited electronic states (from the original NASA Lewis-fit [41] parameters as listed in Table S1 of the supplemental information). Thus, for both models in this section the temperature labeled as T_v will represent a combined vibrational-electronic for the gas mixture and we now evaluate the relaxation term in the modified form as described in Sec. S3.B of the supplemental information.

We first compare the predictions of MMT (solid lines) and Park+M&W (dash-dotted lines) in isothermal heat bath simulations at different temperatures. Results for $T = 8000$ K are shown in Fig. 8, with vibrational temperatures in the upper half and species mole fractions in the lower half. Two sub-plots are shown. In Fig. 8a we compare Park against MMT results including the multi-surface enhancement factors for O₂-dissociation, whereas in Fig. 8b this

factor is absent. The vibrational temperature profiles for MMT and Park show close agreement throughout most of the simulated time, although both MMT curves begin to lag slightly behind Park+M&W the more T_v approaches the heat bath temperature. The gap between MMT and Park roughly coincides with the onset of chemical reactions, as can be seen from the changing mole fractions in the lower half of both sub-figures. Whereas the T_v -profile in the MMT results seems to develop a QSS-like plateau roughly between $t = 1 \mu\text{s}$ and $5 \mu\text{s}$, the vibrational temperature in the Park+M&W case does not and relaxes toward T without interruption.

Differences between Park and MMT become more apparent when comparing mixture composition histories. In Fig. 8a, both models predict a similar early decrease in O_2 mole fraction (dark blue lines), but the differences for N_2 , N and NO are significant. Focusing on nitric oxide first, a small inset in the lower half of Fig. 8a shows a close-up around the time when the NO mole fraction profiles with both models attain their respective peaks. Although there exists little difference in the time when this maximum is reached, the Park+M&W profile (solid green line) peaks at a value only about 25% that of the MMT model (dash-dotted green line). Furthermore, the rate of decline in the NO mole fraction over time is noticeably slower in the MMT model than for Park+M&W.

At this heat bath temperature the Park model also predicts a significantly faster decrease in molecular nitrogen mole fraction (solid red line) than the MMT model (dash-dotted red line). This drop in N_2 is almost exactly mirrored by a faster rise of the atomic nitrogen mole fraction for Park+M&W when compared to MMT (solid vs. dash-dotted orange line). Due to their high activation energies, nitrogen dissociation reactions proceed at rates considerably slower than most other processes in the mixture and most of the N_2 is consumed only after the early significant chemical reactions (O_2 -dissociation and Zeldovich reactions) have already subsided. Thus, differences between the Park and MMT nitrogen profiles at later stages can primarily be traced back to the N_2 -dissociation rates predicted by both models. From the parameters in Table 3 for MMT and those from Table 2 of Ref. [29] for Park, we can estimate that at 8000 K Park's $\text{N}_2 - \text{N}_2$ thermal dissociation rate coefficient is about the same in magnitude as for MMT (see red line in Fig. 10a). However, as shown by the orange line in Fig. 10a, for $\text{N}_2 - \text{N}$ dissociation Park's thermal dissociation rate coefficient is roughly 3.5 times the one predicted for MMT. Therefore, the noticeably faster N_2 dissociation predicted by the Park model relative to MMT can be attributed primarily to the $\text{N}_2 - \text{N}$ reaction.

Figure 8b shows that removing the multi-surface factor from the MMT rates has the overall effect of shifting most of the early reaction dynamics backward by roughly one microsecond. Whereas in Fig. 8a the O_2 mole fraction profiles for Park and MMT were almost identical, without the enhancement factor early O_2 -dissociation is slower, which causes the MMT O_2 mole fraction profile in Fig. 8b to lag behind that of the Park model. This delay has a knock-on effect on the dynamics of all the other species in the MMT result. The decline in N_2 mole fraction is delayed by a similar amount, as is the location of the NO mole fraction peak and the initial rise in both atomic species' mole fractions.

Equivalent results for the $T = 15000 \text{ K}$ case are shown in Figs. 9a and 9b. By comparing the Park and MMT T_v -profiles in the upper half of both sub-plots, one sees that vibrational relaxation again occurs at nearly the same rate

in either of the two MMT and the Park simulations. As before, the MMT profiles exhibit a mild tendency to form a QSS-like plateau, whereas this feature is absent from the Park+M&W profiles. With regard to the evolving mixture composition, differences between both models are clearly visible. Focusing on Fig. 9a first, very early on both the O₂ and N₂ mole fraction profiles in the MMT model (dash-dotted dark blue and red lines) run ahead of their counterparts from the Park model (solid dark blue and red lines). The decrease in molecular nitrogen is mirrored by a rise in atomic nitrogen (orange lines) in both models. Coincidentally, the intersection of N₂ and N mole fraction profiles happens at roughly the same time for MMT (full η_{O_2} factor) and Park. By this time the rate at which N₂ is being consumed is noticeably faster in the Park simulation. Again, this can be attributed mainly to differences in the rate coefficients for nitrogen dissociation in both methods. As time progresses and more N-atoms appear in the mixture, the relative importance to overall N₂ decline gradually shifts from N₂ – N₂ dissociation to N₂ – N dissociation. At $T = 15\,000\text{ K}$ the Park N₂ – N₂ thermal dissociation rate coefficient is about half that in the MMT model, but its N₂ – N dissociation rate coefficient is roughly twice that of MMT (see red and orange lines in Fig. 10a). Thus, it makes sense that the Park simulation exhibits a faster rate of N₂-consumption at the later stages.

Figure 9b shows that removing the multi-surface enhancement factor from the MMT rates delays the early decrease in O₂ mole fraction. Contrary to what could be observed in the comparisons at $T = 8\,000\text{ K}$, at this higher heat bath temperature the MMT and Park profiles now show closer agreement without the η_{O_2} factor. As before, the slower O₂ dissociation without the enhancement factor causes most other changes in the mixture composition to be slightly delayed when compared to Fig. 9a. Nevertheless, differences between Park and MMT are significant with, or without the enhancement factor applied.

Figures 9a and 9b also show clear differences in the amount of nitric oxide being produced between models. Whereas MMT predicts peak NO mole fractions of roughly 0.13, barely any nitric oxide appears in the mixture with the Park model. At this higher heat bath temperature the differences between Park and MMT are even more pronounced than those observed in Figs. 8a and 9b. As before, they can be attributed to significant differences between both models' rate coefficients for the Zeldovich reactions. In Fig. 10b we plot the ratio $k_{\text{Park}}/k_{\text{MMT}}$ for the first Zeldovich reaction $\text{N}_2 + \text{O} \rightarrow \text{NO} + \text{N}$ as the red line. Over the interval $8\,000\text{ K} < T < 15\,000\text{ K}$ this ratio gradually decreases from roughly 0.45 to just above 0.15, which means that at both heat bath temperatures in this comparison the Park model predicts noticeably lower rates for the first Zeldovich reaction than MMT and the amount of nitric oxide produced is correspondingly lower. Simultaneously, the ratio $k_{\text{Park}}/k_{\text{MMT}}$ for the second Zeldovich reaction $\text{NO} + \text{O} \rightarrow \text{O}_2 + \text{N}$ ranges from 0.4 to 0.25 over the same temperature interval (dash-dotted green line in Fig. 10b). This reaction, as written in its endothermic sense, consumes the NO produced via the first Zeldovich reaction. Thus, both NO production and destruction rates via the first and second Zeldovich reactions respectively are significantly lower with the Park rates compared to MMT. Nevertheless, the net effect is that with the Park rates the second reaction remains more active at higher temperatures, rapidly consuming almost all of the NO being produced by the first one. This likely results in the

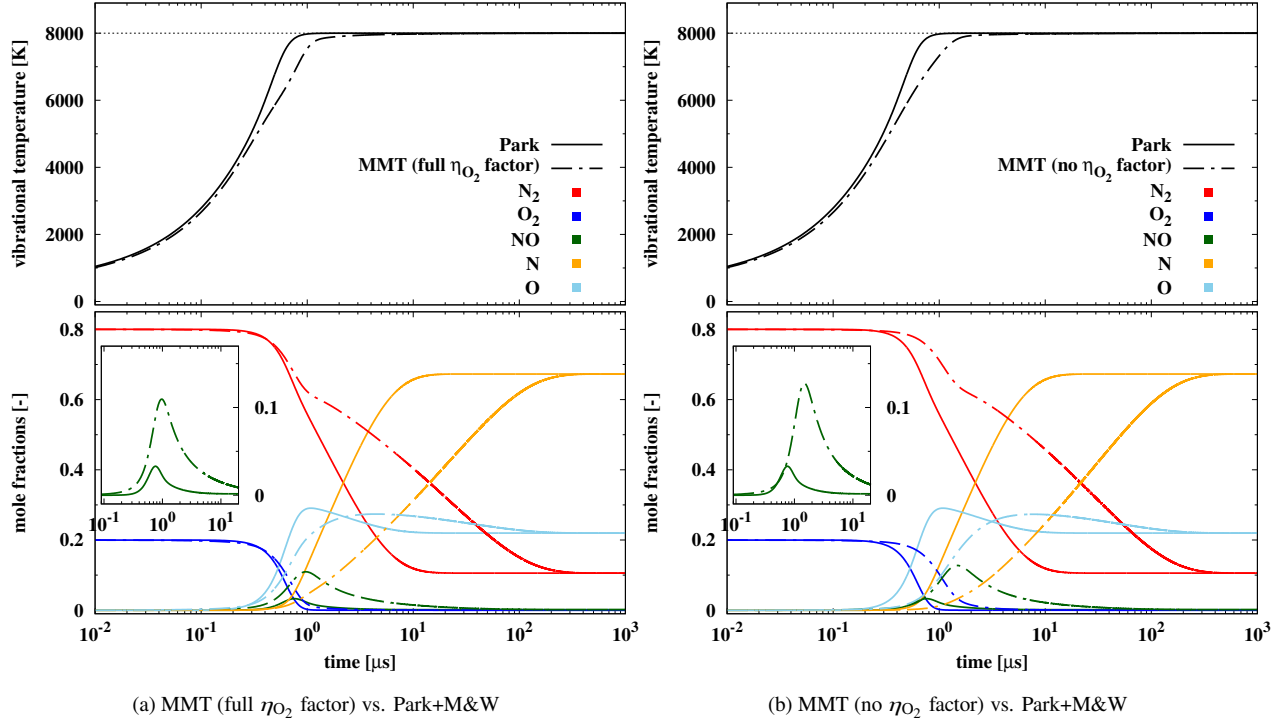


Fig. 8 Isothermal heat bath $T = 8000$ K, complete MMT vs. Park+M&W

much smaller peaks observed of nitric oxide mole fraction in the Park simulations compared to MMT.

Finally, we compare predictions of the MMT and Park models for the two adiabatic heat bath cases listed in Table 4. Results for the lower-enthalpy case are shown in Figs. 11a and 11b (MMT rates with and without multi-surface enhancement factor respectively), with temperature profiles plotted in the upper half and mixture composition below. Focusing on Fig. 11a first, both for Park and MMT we report vibrational (red lines) and trans-rotational (gray lines) temperatures. As was the case in the preceding isothermal cases, here the rates of vibrational relaxation for Park+M&W and MMT are roughly the same. With both models this process is complete after about 20 microseconds. However, one major difference is that the Park+M&W model produces a clearly visible crossing of the T_v and T_{t-r} profiles (solid red vs. gray lines) before relaxing to a common temperature. This feature is absent from the MMT profiles (dash-dotted red vs. gray lines). This overshoot, or lack thereof, may be attributed to differences in how the two source terms Q_v^{relax} and Q_v^{chem} in Eq. (5) of Ref. [14] are computed with both models. In the MMT approach, vibrational relaxation and energy removal rates of a dissociating species have both been calibrated to ab initio data from a common source (see Refs. [23, 24]). Furthermore, Knab's expression for average vibrational energy removed per dissociation, employed in the MMT model (Eq. (16) in Ref. [14]), explicitly includes a dependence on both T_{t-r} and T_v . By contrast, the Park+M&W simulations use non-preferential vibrational energy-chemistry coupling for all species and reactions involved. As Eq. (9) of Ref. [14] shows, with this modeling assumption the average vibrational energy removed in dissociation depends only on T_v and is insensitive to the local trans-rotational temperature. Mole fraction profiles in

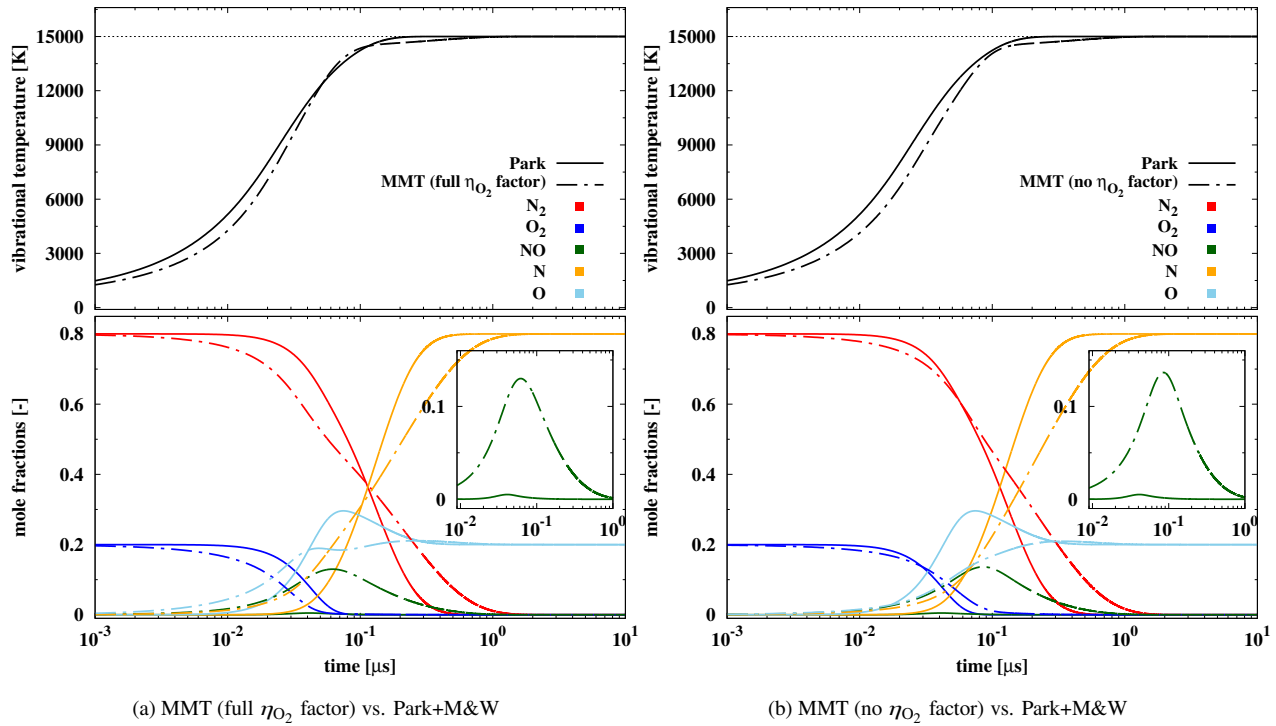


Fig. 9 Isothermal heat bath $T = 15\,000\text{ K}$, complete MMT vs. Park+M&W

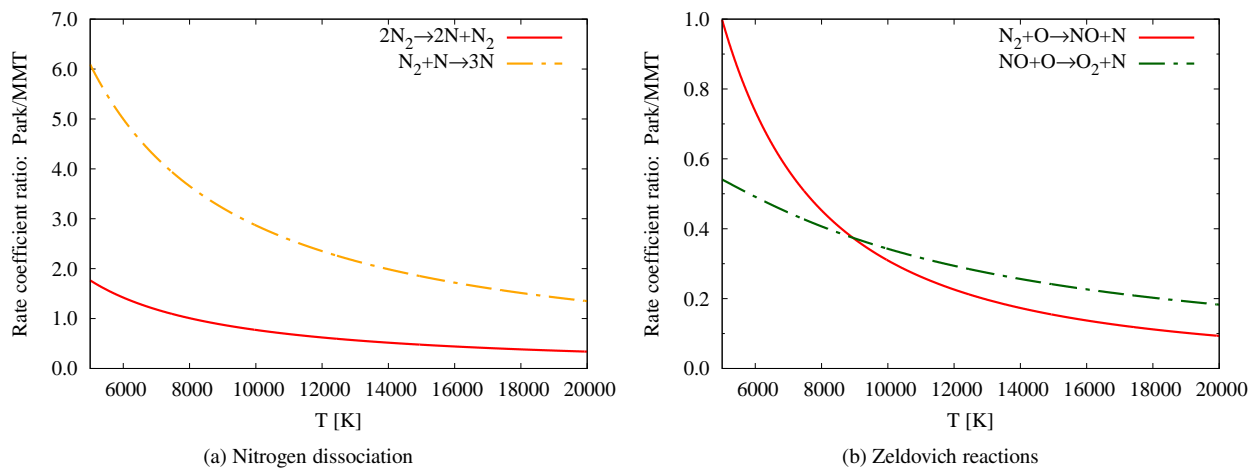


Fig. 10 Ratio of thermal rate coefficients Park/MMT

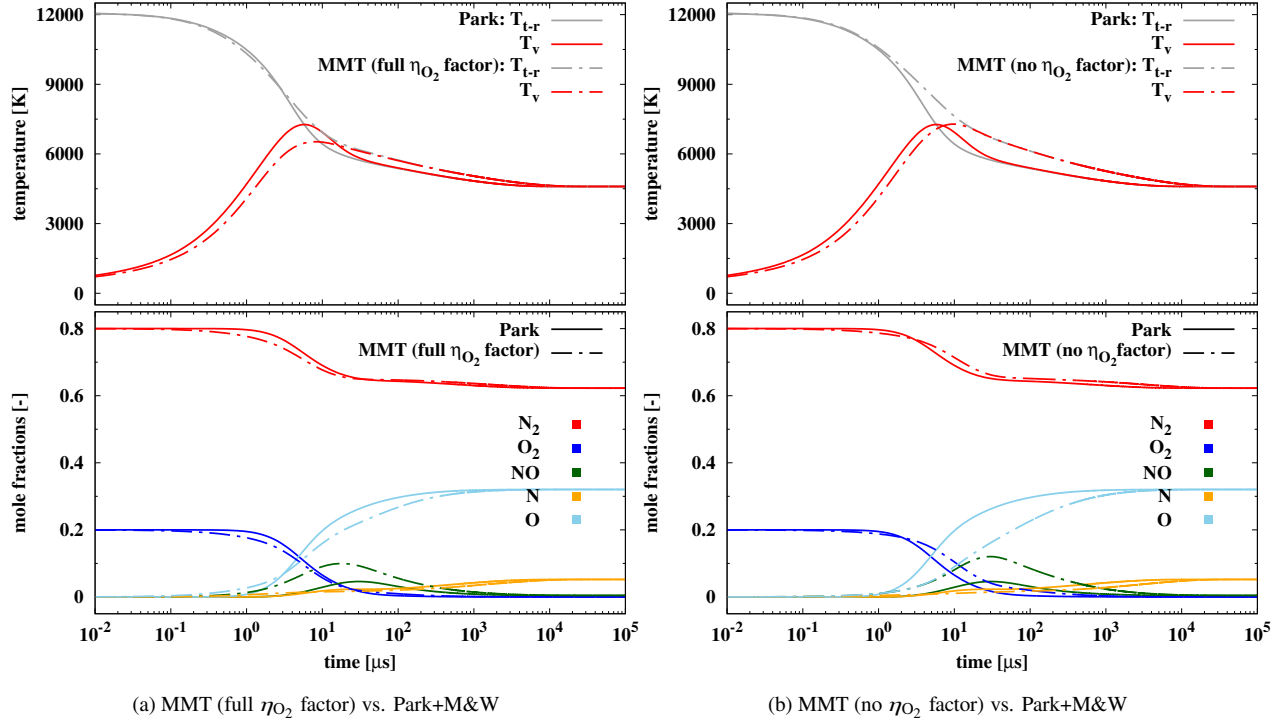


Fig. 11 Adiabatic heat bath $h = 10.1$ MJ/kg, complete MMT vs. Park+M&W

the lower half of Fig. 11a predicted by both models do not differ significantly. Early on, MMT predicts a slightly faster reduction in O_2 and N_2 mole fractions compared to Park, while atomic oxygen production with MMT lags slightly behind the Park profile. The only major discrepancy is again nitric oxide. As seen in the preceding cases, the MMT model predicts a noticeably higher peak in NO mole fraction compared to Park (dash-dotted vs. solid green lines). Figure 11b shows that again, when the MMT model is employed without the multi-surface enhancement factors, all reaction dynamics are slightly delayed. The O_2 mole fraction profiles for MMT (no η_{O_2} factor) now lags slightly behind the Park curve.

Results for the higher-enthalpy case are shown in Figs. 12a and 12b. Most features observed at the lower-enthalpy conditions reappear, but are exacerbated here: The crossing of T_v and T_{t-r} profiles in the Park+M&W profiles (solid red and gray lines) is more severe, while no T_v -overshoot is observed in the MMT result (dash-totted lines). Differences between MMT and Park+M&W in the mixture composition time histories are more noticeable now for all species. At these conditions the MMT model predicts a peak NO mole fraction close to 0.1, whereas with the Park model, practically no nitric oxide is produced.

VII. Conclusions and future work

In this paper we conclude our work detailing all aspects of the newly developed Modified Marrone-Treanor nonequilibrium chemistry model. It follows the model formulation discussed in Ref. [14] by first listing the most

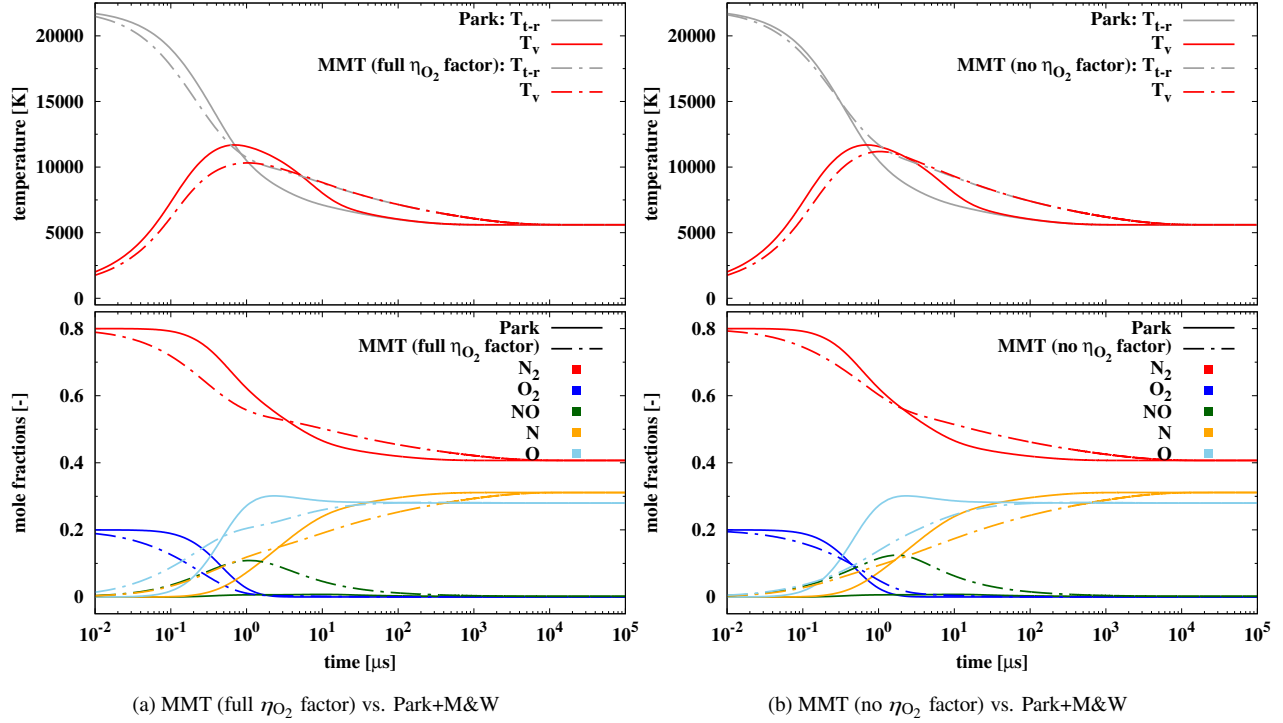


Fig. 12 Adiabatic heat bath $h = 17.9$ MJ/kg, complete MMT vs. Park+M&W

up-to-date vibrational relaxation times and reaction rate parameters for 5-species air mixtures (N_2 , O_2 , NO , N and O), all of them derived from quasiclassical trajectory (QCT) calculations and direct molecular simulations (DMS) on ab initio potential energy surfaces (PESs). The new parameter set allows for computational fluid dynamics (CFD) simulations of high-temperature 5-species air in thermochemical nonequilibrium. The paper presented comparison of CFD-MMT model predictions against DMS reference solutions in space-homogeneous isothermal and adiabatic heat baths representative of post-shock conditions in hypersonic air flows. The MMT model's mutually consistent expressions for nonequilibrium dissociation rate coefficient and associated vibrational energy removal term ensure that the correct amount of energy is transferred between the vibrational and trans-rotational modes at all times. This feature is particularly important for achieving close agreement between CFD-MMT and DMS under adiabatic conditions, where T and T_v both vary in response to chemical reactions altering the gas state. Despite the simplicity of the two-temperature MMT model, remarkable agreement was found with pure ab-initio-based solutions.

We further investigated the implications of employing constant vs. variable non-Boltzmann correction factors in the MMT model. Such variable (i.e. composition-dependent) factors were originally introduced in Ref. [14] to ensure that the MMT model approaches the expected *thermal* dissociation and recombination rates once the gas mixture reaches thermochemical equilibrium. It is found that the overall effect of switching from constant to variable non-Boltzmann factors on the evolution of the gas state is small, as long as reactions are treated as reversible. Since the same factors are applied to forward and backward reaction pairs, changes on the net rates remain minimal.

Results using three MMT parameter sets were presented. The MMT-benchmark parameter set should only be used when comparing to DMS results. The two complete MMT parameter sets are intended for hypersonic CFD simulations, where they represent two limiting assumptions of 1) no oxygen dissociation enhancement due to electronic excitation and 2) full enhancement, described earlier in Sec. II.C.2. Of particular interest was to assess the influence of the theorized multi-surface enhancement factor for oxygen dissociation on the model predictions. As expected, inclusion of the factor significantly speeds up early oxygen dissociation rates and shifts all other dependent reaction dynamics forward in time. Dissociation of O_2 with collision partner N_2 is the most important reaction for producing atomic oxygen early on. As more O-atoms become available, $O_2 + O$ -dissociation also gains in importance. From there on, the two Zeldovich reactions play a central role in shaping the production and consumption rates of all five species. Nitrogen dissociation reactions only become dominant at the very late stages, when most other reactions have subsided.

Finally, a comparison of MMT results against equivalent ones obtained with Park's TT_v model for 5-species air was carried out. At all conditions investigated, the MMT model predicts significantly higher peak mole fractions for nitric oxide than Park. At heat bath temperatures of 10 000 K and below, MMT also predicts noticeably slower conversion of molecular into atomic nitrogen. Both effects can be traced back to the rate parameters for the two Zeldovich reactions ($N_2 + O \rightleftharpoons NO + N$ and $NO + O \rightleftharpoons O_2 + N$). Our new QCT-derived values for these reactions generate noticeably higher rates than those in Park's original 1990 model. The net effect is that far less NO is produced in all Park simulations. In summary, this work demonstrates that the MMT model accurately reproduces all major features present in the DMS reference solutions based on first-principles data. Its computational cost is comparable to Park's model, i.e. orders of magnitude smaller than DMS. This makes it suitable for full-scale CFD simulations of chemically reactive air flows in the hypersonic regime.

Future work to remove some of the MMT model's remaining ad hoc assumptions should include QCT/DMS studies to determine the rates at which excited states of O_2 become populated in shock-heated air and what kind of enhancing effect, if any, this has on the oxygen dissociation rates. Such a study would help narrow down the value of the multi-surface enhancement factor η_{O_2} and whether such a factor should be applied equally to all O_2 -dissociation reactions, or not at all. Computational chemists have already begun generating some of the PESs required for simulating electronically nonadiabatic trajectories in oxygen [42, 43]. Beyond this, additional first-principles studies of non-Boltzmann recombination [44–46] will be required to better justify the limits placed on the variable non-Boltzmann factors in the MMT model.

Acknowledgments

This material is based upon work supported by AFOSR grants FA9550-19-1-0219 and FA9550-23-1-0446, and by NASA grant No. 80NSSC20K1061.

References

- [1] Paukku, Y., Yang, K., Varga, Z., and Truhlar, D., "Global ab initio ground-state potential energy surface of N_4 ," *The Journal of Chemical Physics*, Vol. 139, 2013, p. 044309. doi:10.1063/1.4811653.
- [2] Bender, J., Valentini, P., Nompelis, I., Paukku, Y., Varga, Z., Truhlar, D., Schwartzentruber, T., and Candler, G., "An improved potential energy surface and multi-temperature quasiclassical trajectory calculations of $N_2 + N_2$ dissociation reactions," *The Journal of Chemical Physics*, Vol. 143, 2015, p. 054304. doi:10.1063/1.4927571.
- [3] Lin, W., Varga, Z., Song, G., Paukku, Y., and Truhlar, D., "Global triplet potential energy surfaces for the $N_2(X^1\Sigma) + O(^3P) \rightarrow NO(X^2\Pi) + N(^4S)$ reaction," *The Journal of Chemical Physics*, Vol. 144, 2016, p. 024309. doi:10.1063/1.4938241.
- [4] Varga, Z., Meana-Pañeda, R., Song, G., Paukku, Y., and Truhlar, D., "Potential energy surface of triplet N_2O_2 ," *The Journal of chemical physics*, Vol. 144, No. 2, 2016, p. 024310. doi:10.1063/1.4939008.
- [5] Paukku, Y., Yang, K., Varga, Z., Song, G., Bender, J., and Truhlar, D., "Potential energy surfaces of quintet and singlet O_4 ," *The Journal of Chemical Physics*, Vol. 147, 2017, p. 034301. doi:10.1063/1.4993624.
- [6] Varga, Z., Paukku, Y., and Truhlar, D., "Potential energy surfaces for $O + O_2$ collisions," *The Journal of Chemical Physics*, Vol. 147, 2017, p. 154312. doi:10.1063/1.4997169.
- [7] Paukku, Y., Varga, Z., and Truhlar, D., "Potential energy surface of triplet O_4 ," *The Journal of Chemical Physics*, Vol. 148, 2018, p. 124314. doi:10.1063/1.5017489.
- [8] Li, J., Varga, Z., Truhlar, D., and Guo, H., "Many-body permutationally invariant polynomial neural network potential energy surface for N_4 ," *Journal of Chemical Theory and Computation*, Vol. 16, No. 8, 2020, pp. 4822–4832. doi:10.1021/acs.jctc.0c00430.
- [9] Varga, Z., Liu, Y., Li, J., Paukku, Y., Guo, H., and Truhlar, D., "Potential energy surfaces for high-energy $N + O_2$ collisions," *The Journal of Chemical Physics*, Vol. 154, No. 8, 2021, p. 084304. doi:10.1063/5.0039771.
- [10] Varga, Z., and Truhlar, D., "Potential energy surface for high-energy $N + N_2$ collisions," *Phys. Chem. Chem. Phys.*, Vol. 23, 2021, pp. 26273–26284. doi:10.1039/D1CP04373K.
- [11] Varga, Z., Meana-Pañeda, R., Song, G., Paukku, Y., and Truhlar, D. G., "POTLIB: An Online Library of Potential Energy Surfaces," 2021. URL comp.chem.umn.edu/potlib/.
- [12] Truhlar, D., and Muckerman, J., "Reactive scattering cross sections III: Quasiclassical and semiclassical methods," *Atom-Molecule Collision Theory*, Springer, 1979, pp. 505–566.
- [13] Chaudhry, R., Bender, J., Schwartzentruber, T., and Candler, G., "Quasiclassical Trajectory Analysis of Nitrogen for High-Temperature Chemical Kinetics," *Journal of Thermophysics and Heat Transfer*, Vol. 32, No. 4, 2018, pp. 833–845. doi:10.2514/1.T5484.

- [14] Chaudhry, R. S., Torres, E., Schwartzentruber, T. E., and Candler, G., “Modified Marrone-Treanor dissociation model: formulation and verification for diatom/atom mixtures,” 2025. URL <http://arxiv.org/abs/2506.06236>, submitted for review, preprint available on arxiv.org.
- [15] Bird, G., *Molecular Gas Dynamics and the Direct Simulation of Gas Flows*, Oxford University Press, 1994.
- [16] Koura, K., “Monte Carlo direct simulation of rotational relaxation of nitrogen through high total temperature shock waves using classical trajectory calculations,” *Physics of Fluids*, Vol. 10, 1998, p. 2689.
- [17] Valentini, P., Schwartzentruber, T., Bender, J., Nompelis, I., and Candler, G., “Direct molecular simulation of nitrogen dissociation based on an ab initio potential energy surface,” *Physics of Fluids*, Vol. 27, 2015, p. 086102. doi:10.1063/1.4929394.
- [18] Valentini, P., Schwartzentruber, T., Bender, J., and Candler, G., “Dynamics of nitrogen dissociation from direct molecular simulation,” *Physical Review Fluids*, Vol. 1, 2016, p. 043402. doi:10.1103/PhysRevFluids.1.043402.
- [19] Grover, M. S., Verhoff, A. M., Valentini, P., and Bisek, N. J., “First principles simulation of reacting hypersonic flow over a blunt wedge,” *Physics of Fluids*, Vol. 35, No. 8, 2023, p. 086106. doi:10.1063/5.0161570, URL <https://doi.org/10.1063/5.0161570>.
- [20] Grover, M., Schwartzentruber, T., Varga, Z., and Truhlar, D., “Vibrational Energy Transfer and Collision-Induced Dissociation in O + O₂ Collisions,” *Journal of Thermophysics and Heat Transfer*, Vol. 33, No. 3, 2019, pp. 797–807. doi:10.2514/1.T5551.
- [21] Grover, M., Torres, E., and Schwartzentruber, T., “Direct molecular simulation of internal energy relaxation and dissociation in oxygen,” *Physics of Fluids*, Vol. 31, 2019, p. 076107. doi:10.1063/1.5108666.
- [22] Torres, E., and Schwartzentruber, T., “Direct molecular simulation of oxygen dissociation across normal shocks,” *Theoretical and Computational Fluid Dynamics*, Vol. 36, No. 1, 2022, pp. 41–80. doi:10.1007/s00162-021-00596-6.
- [23] Torres, E., Geistfeld, E. C., and Schwartzentruber, T. E., “High-Temperature Nonequilibrium Air Chemistry from First Principles,” *Journal of Thermophysics and Heat Transfer*, Vol. 38, No. 2, 2024, pp. 260–291. doi:10.2514/1.T6863.
- [24] Torres, E., and Schwartzentruber, T. E., “Characteristic vibrational and rotational relaxation times for air species from first-principles calculations,” *Journal of Thermophysics and Heat Transfer*, Vol. 39, No. 2, 2025, pp. 223–249. doi:10.2514/1.T7042.
- [25] Valentini, P., Grover, M. S., and Bisek, N. J., “Toward ab initio molecular simulation of reacting air: Mach 15 air flow over a blunt wedge,” *Journal of Fluid Mechanics*, Vol. 997, 2024, p. A27. doi:10.1017/jfm.2024.772.
- [26] Schwartzentruber, T., Grover, M., and Valentini, P., “Direct Molecular Simulation of Nonequilibrium Dilute Gases,” *Journal of Thermophysics and Heat Transfer*, Vol. 32, No. 4, 2018, pp. 892–903. doi:10.2514/1.T5188.
- [27] Park, C., *Nonequilibrium hypersonic aerothermodynamics*, Wiley, New York, 1990.
- [28] Millikan, R. C., and White, D. R., “Systematics of Vibrational Relaxation,” *The Journal of Chemical Physics*, Vol. 39, No. 12, 1963, pp. 3209–3213. doi:10.1063/1.1734182.

- [29] Park, C., "Review of chemical-kinetic problems of future NASA missions. I - Earth entries," *Journal of Thermophysics and Heat Transfer*, Vol. 7, No. 3, 1993, pp. 385–398. doi:10.2514/3.431.
- [30] Ibraguimova, L. B., Sergievskaya, A. L., Levashov, V. Y., Shatalov, O. P., Tunik, Y. V., and Zabelinskii, I. E., "Investigation of oxygen dissociation and vibrational relaxation at temperatures 4000-10800 K," *The Journal of Chemical Physics*, Vol. 139, No. 3, 2013, p. 034317. doi:10.1063/1.4813070.
- [31] Streicher, J. W., Krish, A., and Hanson, R. K., "Vibrational relaxation time measurements in shock-heated oxygen and air from 2000 K to 9000 K using ultraviolet laser absorption," *Physics of Fluids*, Vol. 32, No. 8, 2020, p. 086101. doi:10.1063/5.0015890.
- [32] Streicher, J., Krish, A., and Hanson, R., "Coupled vibration-dissociation time-histories and rate measurements in shock-heated, nondilute O₂ and O₂ – Ar mixtures from 6000 to 14000 K," *Physics of Fluids*, Vol. 33, No. 5, 2021, p. 056107. doi:10.1063/5.0048059.
- [33] Streicher, J. W., Krish, A., and Hanson, R. K., "High-temperature vibrational relaxation and decomposition of shock-heated nitric oxide. I. Argon dilution from 2200 to 8700 K," *Physics of Fluids*, Vol. 34, No. 11, 2022, p. 116122. doi:10.1063/5.0109109.
- [34] Streicher, J. W., Krish, A., and Hanson, R. K., "High-temperature vibrational relaxation and decomposition of shock-heated nitric oxide: II. Nitrogen dilution from 1900 to 8200 K," *Physics of Fluids*, Vol. 34, No. 11, 2022, p. 116123. doi:10.1063/5.0122787.
- [35] Marrone, P., and Treanor, C., "Chemical Relaxation with Preferential Dissociation from Excited Vibrational Levels," *The Physics of Fluids*, Vol. 6, 1963, p. 1215.
- [36] Chaudhry, R., "Modeling and Analysis of Chemical Kinetics for Hypersonic Flows in Air," , 2018. URL <https://hdl.handle.net/11299/201709>, University of Minnesota - Doctoral Thesis.
- [37] Nikitin, E., *Theory of elementary atomic and molecular processes in gases*, 1974.
- [38] Park, C., *Two-temperature interpretation of dissociation rate data for N₂ and O₂*, 1988. doi:10.2514/6.1988-458, URL <https://arc.aiaa.org/doi/abs/10.2514/6.1988-458>.
- [39] Sharma, S. P., Huo, W. M., and Park, C., "Rate parameters for coupled vibration-dissociation in a generalized SSH approximation," *Journal of Thermophysics and Heat Transfer*, Vol. 6, No. 1, 1992, pp. 9–21. doi:10.2514/3.312, URL <https://doi.org/10.2514/3.312>.
- [40] Park, C., *Problems of rate chemistry in the flight regimes of aeroassisted orbital transfer vehicles*, 1984. doi:10.2514/6.1984-1730, AIAA 84-1730.
- [41] McBride, B., Gordon, S., and Reno, M., "Coefficients for Calculating Thermodynamic and Transport Properties of Individual Species," Tech. rep., NASA Technical Memorandum 4513, 1993.

- [42] Varga, Z., Shu, Y., Ning, J., and Truhlar, D., "Diabatic Potential Energy Surfaces and Semiclassical Multi-State Dynamics for Fourteen Coupled 3A' States of O₃," *Electronic Structure*, Vol. 4, No. 4, 2022, p. 047002. doi:10.1088/2516-1075/ac94ac.
- [43] Shu, Y., Varga, Z., Kanchanakungwankul, S., Zhang, L., and Truhlar, D. G., "Diabatic States of Molecules," *The Journal of Physical Chemistry A*, Vol. 126, No. 7, 2022, pp. 992–1018. doi:10.1021/acs.jpca.1c10583.
- [44] Geistfeld, E. C., Torres, E., and Schwartzentruber, T., "Quasi-classical trajectory analysis of three-body collision induced recombination in neutral nitrogen and oxygen," *The Journal of Chemical Physics*, Vol. 159, No. 15, 2023, p. 154111. doi:10.1063/5.0163942.
- [45] Pahlani, G., Torres, E., Schwartzentruber, T., and James, R. D., "Objective molecular dynamics investigation of dissociation and recombination kinetics in high-temperature nitrogen," *Physics of Fluids*, Vol. 35, No. 6, 2023, p. 067111. doi:10.1063/5.0150492.
- [46] Macdonald, R. L., "State-to-state study of non-equilibrium recombination of oxygen and nitrogen molecules," *The Journal of Chemical Physics*, Vol. 160, No. 13, 2024, p. 134307. doi:10.1063/5.0195238.